SPECTROSCOPY OF NEUTRAL MERCURY IN A MAGNETO-OPTICAL TRAP BASED ON A NOVEL YTTERBIUM FIBER-AMPLIFIED COOLING LASER SOURCE

by

Christian Robert Lytle

A Dissertation Submitted to the Faculty of the

COLLEGE OF OPTICAL SCIENCES

In Partial Fulfillment of the Requirements
For the Degree of

DOCTOR OF PHILOSOPHY

In the Graduate College

THE UNIVERSITY OF ARIZONA

2 0 1 6

THE UNIVERSITY OF ARIZONA
GRADUATE COLLEGE

As members of the Final Examination Committee, we certify that we have read the dissertation prepared by Christian Robert Lytle
entitled Spectroscopy of Neutral Mercury in a Magneto-Optical Trap based on a Novel Ytterbium Fiber-Amplified Cooling Laser Source
and recommend that it be accepted as fulfilling the dissertation requirement for the Degree of Doctor of Philosophy.

Date: 13 July 2016
R. Jason Jones

Date: 13 July 2016
Brian P. Anderson

Date: 13 July 2016
Alexander Cronin

Final approval and acceptance of this dissertation is contingent upon the candidate's submission of the final copies of the dissertation to the Graduate College.

I hereby certify that I have read this dissertation prepared under my direction and recommend that it be accepted as fulfilling the dissertation requirement.

Date: 13 July 2016
Dissertation Director: R. Jason Jones

STATEMENT BY AUTHOR

This dissertation has been submitted in partial fulfillment of requirements for an advanced degree at The University of Arizona and is deposited in the University Library to be made available to borrowers under rules of the Library.

Brief quotations from this dissertation are allowable without special permission, provided that accurate acknowledgment of source is made. Requests for permission for extended quotation from or reproduction of this manuscript in whole or in part may be granted by the head of the major department or the Dean of the Graduate College when in his or her judgment the proposed use of the material is in the interests of scholarship. In all other instances, however, permission must be obtained from the author.

SIGNED: Christian Robert Lytle

ACKNOWLEDGEMENTS

Over the many years of working on the mercury optical clock project, many people, inside and outside the lab, have been supportive of my endeavors. Justin Paul, who I worked alongside for six years, is a fantastic experimentalist, and the many creative techniques and methods he contributed were essential to moving the project forward. I would also like to thank Tsung-han and David Carlson for their assistance over the years. Tsung-han in particular was tremendously helpful in dealing with fiber issues. I would also like to highlight our collaborations with Professor Long-sheng Ma at East China Normal University in Shanghai. During the 6 months Su Fang was working in our lab, she was invaluable in building the ultra-stable system and assisting in the search for the clock transition. I would also like to thank Professor Ma for facilitating my work in their lab during the summer of 2012.

To my advisor Jason Jones, thank you for your mentorship over the years. Your deep understanding of scientific principles and experimental physics has been of tremendous value to this project. The mercury project has brought with it significant technical challenges in many areas, from optics to electronics to machining to vacuum systems. Along the way, you have provided valuable insight into all these areas, and helped smooth out many bumps along the road. I am grateful for the opportunity to work with you.

Beyond the lab, classwork and the many long days of research, there have been several friendships which have been invaluable to my sanity and motivation. To Kevin Andrade, thanks for all the great times hanging out in Tucson and for introducing me to real hip-hop. To Van Chounlamountry, Mike Danielson, and Mitch Seiffert: you have all been tremendous friends since college, and the effort you all made to stay connected over the many years since graduating has deeply impacted my life. I look forward to many more years of friendship.

Finally, I want to thank my family for their unwavering support over the years. I would not have completed this degree without their love and encouragement.

DEDICATION

To my family and friends that have supported me through this endeavor.

TABLE OF CONTENTS

TABLE OF CONTENTS – *Continued*

LIST OF FIGURES

LIST OF FIGURES – *Continued*

ABSTRACT

In this dissertation I present experimental results obtained on the mercury optical clock project in the research group of Jason Jones at the University of Arizona. The project began in 2008 with the purpose of investigating the feasability of neutral mercury as an optical clock species. The first series of investigations involved building the essential apparatus and scanning the doppler-broadened 6^1S_0 - 6^3P_0 clock transition in ^{199}Hg. Here I present significant modifications to the cooling and trapping laser, improvements to the spectroscopy laser linewidth, and attempts to measure the 2-photon transition in ^{199}Hg.

After previously demonstrating spectroscopy of the mercury clock transition using an optically-pumped semiconductor laser for the cooling and trapping source (OPSL), we replaced the OPSL with a a fiber-amplified ECLD system. We custom built a fiber amplifier to provide gain at 1015 nm, demonstrating the system can yield up to 5 W of signal power with excellent suppression of the ASE power. We find that the ASE is well suppressed by using a two-stage configuration and short sections of gain fiber.

The linewidth of our original spectroscopy laser was over 10 kHz, which is unsuitable to resolve of sub-Doppler features. To enhance the performance of our spectroscopy system, we integrated faster feedback bandwidth using AOMs, and incorporated derivative gain into the system. This resulted in a feedback bandwidth for our spectroscopy laser of over 200 kHz. With this system, we demonstrate an

actively stabilized linewidth of 525 Hz for our spectroscopy system.

Using the upgraded cooling and spectroscopy laser systems, we demonstrate spectroscopy of the clock system and confirm temperature measurements derived from the transition linewidth. We also describe attempts to detect the recoil shift and 2-photon transition in neutral mercury.

CHAPTER 1

Introduction: precision timekeeping and the age of optical atomic clocks

1.1 Timekeeping: past to present

Inventing ways to delineate and mark the passage of time in increasingly precise increments has been a constant source of inspiration to humanity. The rotation of earth itself yields the most basic clock derived from nature: the rising and setting of the sun, moon, and constellations. Many early civilizations exploited the constant burn rate of a candle or the periodic drips from a water clock to measure ever smaller increments of time. Throughout history, clocks have also been an important aid to navigation [1]. In the 20th century, timekeeping technology has progressed rapidly, providing an essential foundation for many modern technologies, not the least of which is GPS [2]. This 20th century revolution began with the invention of quartz crystal oscillators [3] and culminated with the development of the atomic clock. In this chapter we provide a basic theoretical background and motivation for the development of optical atomic clocks. We also highlight the reasons for specifically investigating mercury.

1.2 Stability of atomic clocks

Any type of clock relies on a standard to minimize variations in the oscillator period. In a pendulum clock, that standard is usually a gravitational field; in a quartz

clock, the standard is the vibrational modes in the crystal lattice. In an atom, we can use the well-defined energy levels as a stable oscillator reference [4]. The first atomic clock, the cesium maser, used a coherent microwave source (maser) to probe the ground state transition of cesium [5]. Iterations and improvements to that first design have yielded both the NIST F1 and F2 fountain clocks, which use lasers to prepare the atoms prior to interrogation by the microwave source. The international standard for the duration of the second is defined as 9,192,631,770 oscillations between two hyperfine ground states of the cesium-133 atom [6]. The NIST F2 in Boulder, CO is the most recent cesium standard, established in 2014.

Although the cesium clock remains the current internationally recognized standard for the second, the long term stability of the cesium standard is a few orders of magnitude below the stability level provided by the current generation of research grade atomic clocks. Research clock systems now inhabit the optical domain, where the naturally high frequency considerably boosts the long term frequency stability.

A clock is largely defined by two parameters, the uncertainty and the stability. The uncertainty is the difference between the clock frequency and a known, unperturbed frequency standard. This difference will be influenced by several systematic effects, including oscillator measurement error and external fields perturbing the atomic resonance. Systematic shifts include doppler shifts, stark shifts, and Zeeman shifts.

An even better method to characterize a clock is the fractional frequency stability [7]. The fractional frequency stability quantifies fluctuations of the clock oscillator relative to its operating frequency, rather than an absolute external standard. In a

clock system, the fractional frequency stability is represented by the Allan variance [8–10]:

$$\sigma_y^2(\tau) = \frac{1}{2(M-1)} \sum_{i=1}^{M-1} [\langle y(\tau) \rangle_{i+1} - \langle y(\tau) \rangle_i]^2, \tag{1.1}$$

where $y(\tau)$ is the fractional frequency difference as a function of the interval τ. Ideally, the quantity $\sigma_y^2(\tau)$ will decrease over long averaging times. We can express the Allan deviation in terms of specific clock parameters to elucidate the noise processes which may limit stability [11]:

$$\sigma_y(\tau) = \frac{1}{\pi Q} \sqrt{\frac{T_c}{\tau}} \left(\frac{1}{N} + \frac{1}{N n_{ph}} + \frac{2\sigma_N^2}{N} + \gamma \right)^{1/2} \tag{1.2}$$

where each term in parenthesis is the signal-to-noise ratio (SNR) for a specific noise process. As for the individual parameters in Eq. 1.2, T_c is the period during which the atoms are interrogated, N is the atom number, n_{ph} is the number of detected photons, σ_N is the fluctuation of the atom number and γ is the frequency noise of the probe laser. The first term represents the fundamental quantum projection noise [12]. The second term is the measurement photon shot noise, and, for large numbers of collected photons per atom, is typically well below the projection noise. The third term is the noise resulting from fluctuations in the atom number during each measurement period T_c. It can be minimized by using appropriate detection techniques [11]. The fourth term is from frequency noise on the probe laser. The most pernicious probe noise is that which is periodic with the measurement cycle T_c, contributing to the so called Dick effect.

Assuming white noise is dominant, we can simplify Eq. 1.2 down to the quantum

projection noise (QPN):

$$\sigma_y(\tau) \approx \frac{1}{\pi}\frac{\delta\nu}{\nu_0}\sqrt{\frac{T_c}{\tau N}}, \tag{1.3}$$

where the factor $\frac{\delta\nu}{\nu_0}$ is the ratio of the linewidth to the absolute transition frequency. To decrease $\sigma_y(\tau)$ we want to minimize this factor, implying a high absolute frequency and very narrow linewidth of the clock transition. This motivates the pursuit of optical clock standards over the past two decades. The relatively high frequencies and narrow-linewidth transitions yield a strong natural advantage over the microwave standards [13].

1.3 Measuring the clock transition frequency

Despite the inherent advantages of optical atomic clocks, one problem hindered significant progress in the optical clock field for several decades. To evaluate the stability of a clock, the clock frequency must be measured relative to a separate standard with a known stability. The span between the microwave domain and the optical domain is hundreds of terahertz, a value which cannot be directly counted by any modern electronics. To span this large frequency gap, many previous research efforts implemented extensive chains of phase-locked oscillators, gradually stepping from the microwave region to the visible region [14, 15]. Unfortunately, such systems required a high level of expense and complexity. With the development of the frequency comb [16, 17], direct measurement of optical frequencies has become a relatively straightforward process [18–20].

The optical frequency comb is a mode-locked femtosecond laser, in which two degrees-of-freedom of the system are stabilized: the relative phase between the pulse

envelope and the carrier wave, and the pulse repetition rate (f_{REP}). The former is generally referred to as the cavity envelope offset frequency (f_{CEO}). Applying a Fourier transform to this stabilized ultrafast pulse train, the output in frequency space then consists of a series of single-frequency modes which form a comb structure. All of the comb modes are phase coherent with eachother, and this property allows the comb to span the gap between microwave and optical sources. Therefore, if we can count the microwave frequency, we can extract the optical frequency. The comb has greatly simplified many types of phase-coherent spectroscopy measurements across frequency domains [21, 22].

1.4 Optical clock overview: ion clocks and neutral atom clocks

Optical clock research accelerated in the late 1990's with the advent of the frequency comb. Atomic clocks based on ions were explored in-depth during the early days of clock research, due largely to the fact that ion trapping is generally simpler and more robust than neutral atom trapping. Ions clocks also have lower sensitivity to frequency shifts and noise from external fields [23]. However, the fractional frequency stability of ion clocks is limited by the inability to trap large numbers of ions. It is much easier to increase the SNR in neutral clocks by trapping large numbers of atoms.

In ion clocks, a single ion is confined in a Paul trap and probed with a narrow-linewidth spectroscopy laser. Several species have been investigated as potential ion frequency standards, including Al^+, $^{40}Ca^+$, Yb^+, $^{88}Sr^+$, and $^{199}Hg^+$ [24–28]. One of the most accurate ion clocks to date, the quantum logic Al^+ clock, exhibits a

fractional frequency stability of 8.6×10^{-18} [24].

Neutral atom clocks, as noted previously, show significant potential for reaching low levels of frequency stability. Ion clocks often require months of averaging time to reach 10^{-18} stability levels. Utilizing high atom numbers, neutral atoms can reach the same stability levels on the order of hours. However, this performance comes at the cost of much greater experimental complexity. Several of the most promising types of neutral clocks require two-stage Doppler cooling and lattice traps in order to minimize noise in the clock state. The lattice is generated using a high-intensity laser tuned to the magic-wavelength, where the stark shifts of the ground and excited states cancel. Since neutral clocks are more susceptible to external perturbations, significant research effort went into resolving blackbody stark shifts of the clock state in strontium and ytterbium. Now that this blackbody problem has been solved, the main factor preventing these clock from reaching the quantum projection noise limit lies in the oscillator noise. The current record for neutral clock stability has been measured at 1.6×10^{-18}, averaged over 25,000 seconds [7].

1.5 Advantages of a mercury neutral atom clock

The energy level structure of neutral mercury, shown in Figure 1.1, is similar to other alkaline-earth elements such as ytterbium and strontium. The doubly-forbidden $^1S_0$ - $^3P_0$ transition, weakly allowed in fermionic isotopes by way of nuclear spin-orbit coupling, has a natural linewidth of approximately 100 mHz. With a wavelength of 265.6 nm, the narrow linewidth and high frequency of this transition shows strong potential for excellent long-term frequency stability (see Eq. 1.2). In addition, anal-

ysis of the blackbody stark shift of mercury has shown susceptibilities to blackbody noise nearly an order-of-magnitude lower than strontium and ytterbium [29].

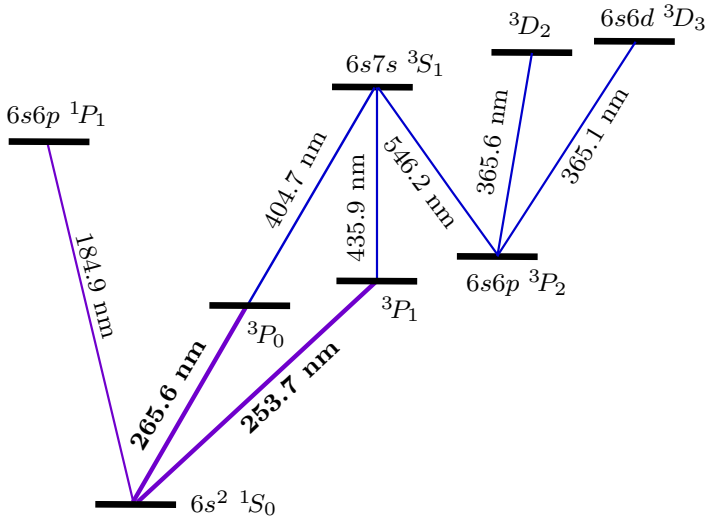

Figure 1.1: Energy level structure of mercury.

The desirability of mercury as an optical clock species is further enhanced by several technical implementation advantages. The linewidth of the intercombination $^1S_0$ - $^3P_1$ cooling transition is 1.3 MHz, which results in a reasonable Doppler-limited temperature of 31 µK. This is a suitable Doppler temperature for efficient loading of a lattice trap, eliminating the need for multi-stage Doppler cooling on the $^1P_1$ line. This also obviates the immense technical challenge of generating laser light at 185 nm, the wavelength of the $^1P_1$ line. Because mercury has a very high vapor pressure, no oven is required to fill the trapping chamber with vapor. Several other clock species have been hindered by the requirement of having to place a powerful blackbody source (i.e. oven) so close to the experiment. Finally, the high atomic weight of mercury should reduce its susceptibility to motion-induced shifts in a

lattice trap.

Despite the advantages, there are a few prominent downsides which have become apparent in the mercury clocks built to-date. These problems are related to the challenge of developing the custom UV laser sources required for mercury. In addition to the technical challenges involved, ultraviolet light damages most types of optics over time, and the damage scales with the intensity. This results in the need for frequent realignment and replacement of optics in the cooling laser system and the lattice laser systems. A significant portion of this dissertation is dedicated to describing the development of the laser sources used in our mercury clock experiment.

1.6 Details of mercury isotopes and highlights of current clock systems

The $^1S_0$ - $^3P_0$ transition is allowed by way of the hyperfine interaction, which creates an admixture of the $^1P_1$ and $^3P_0$ states. Since the $^1P_1$ state is an allowed via spin-orbit coupling, transitions to the $^3P_0$ become weakly allowed with the state mixture. This mixture only occurs for nuclear spin states F = 1/2 (^{199}Hg) and F = 3/2 (^{201}Hg). The rest of the mercury isotopes are bosons with zero spin. The only method available for exciting the clock transition in the bosons is via state quenching with an externally applied DC magnetic field. In this dissertation we focus on spectroscopy of ^{199}Hg.

Currently, two complete mercury lattice systems exist. The first successful mercury magneto-optical trap was built by Katori in 2008 [29], and since then, they have implemented a full mercury lattice system. Most recently, they have compared their mercury clock to an ^{87}Sr standard [30]. This measurement pinned the systematic

uncertainty at 7.2×10^{-17} and the fractional stability at $3 \times 10^{-15}/\sqrt{\tau}$. The group of Sebastian Bize at LNE-SYRTE in Paris have also implemented a complete lattice clock based on mercury [31–33]. Their most recent results yield an uncertainty of 5.7×10^{-15} and a frequency stability of $5.4 \times 10^{-15}/\sqrt{\tau}$ [34].

1.7 Overview of dissertation

This dissertation describes our process building the components of a mercury clock system. In Chapter 2, I describe our first generation cooling laser system, used to trap and cool the mercury atoms. This system was based on OPSL/VECSEL technology. I also describe our method for locking to the mercury cooling transition. In Chapter 3, I discuss the second generation cooling system, based on a novel fiber-amplified ECLD. Chapter 4 discusses the process of constructing the mercury MOT chamber and the magnetic field coils. In Chapter 5 I describe the measurements used to characterize the MOT. Chapter 6 details all the components of the spectroscopy system, including the laser setup, the cavity referencing system, the spectroscopy measurements, and our attempts to measure the recoil doublet and the two-photon transition.

CHAPTER 2

First generation MOT cooling laser: OPSL source

The laser cooling apparatus is a critical component of an optical clock experiment. To drive the 6^1S_0 - 6^3P_1 cooling transition in neutral Hg, we require a laser source with a linewidth less than the 1.27 MHz linewidth of the cooling transition, and a tuning range of at least 80 GHz, the approximate frequency span of the common mercury isotopes. We also need a source which can generate a minimum of 100 mW at 253.7 nm. Since there are no commercial UV systems which could satisfy these requirements, we decided the best route would be to implement a frequency conversion scheme for an IR source at 1015 nm. ECLD sources excel in applications requiring tunability and a reasonably narrow linewidths, but suffer from poor beam profiles. Other groups have used solid-state disc lasers [29, 32, 35], but these can be prone to damage at high powers. We decided to use an optically-pumped semiconductor laser (OPSL). OPSL devices are a type of optically-pumped vertical external cavity surface-emitting (VECSEL) laser, and have been shown to be highly versatile laser sources for atomic spectroscopy [36–38].

2.1 OPSL device characteristics

We chose the OPSL device because of a unique blend of characteristics which make it well suited to atomic spectroscopy work. These devices combine some of the best

properties of diode lasers and solid-state lasers, namely, high-power, tunability and clean spatial mode profiles [39–41]. Using modern materials science methods, the emission spectrum of OPSLs can be engineered over a wide range of wavelengths, providing access to wavelengths unreachable by solid-state lasers [42, 43]. Experiments have also demonstrated OPSL devices with narrow linewidths, as well as mode-locking capabilities [44–46]. With the ability to draw upon in-house expertise in OPSL design from Yuishi Kaneda and his research group at Optical Sciences [47], implementing a frequency-quadrupled OPSL laser cooling source was an easy choice.

An OPSL is a quantum-well semiconductor device placed on a top of a distributed bragg reflector mirror (DBR). The quantum-wells form a resonant periodic gain (RPG) structure, and are grown using InGaAs. This RPG structure is then layered on the DBR mirror. An additional layer of InGaP material provides the endcap and air-interface, forming the other end of the so-called microcavity [48] RPG region. This endcap can be AR-coated or left uncoated, resulting in slight changes to the external cavity dynamics. The RPG structure will expand and contract with temperature, providing the device with potent temperature tuning capabilities. As a corollary to this, it is important to temperature stabilize the device to achieve stable frequency operation.

2.2 OPSL construction

The OPSL, by its nature, requires an external cavity in order to lase. Figure 2.1 shows the OPSL device mounted at one end of a laser resonator, positioned at the resonator waist. To ensure temperature stability and safe operation of the device,

we mount the OPSL on a large liquid cooling block. This allows us to vary the chip temperature between 5 °C and 25 °C, and provide a basic level of temperature stabilization. The water chiller supplying the cooling block has a long time settling constant, which can be a hindrance to time-efficient day-to-day operation of the device. The settling time constant could be improved by attaching the device to a peltier device, but the water chiller proved sufficient for our application.

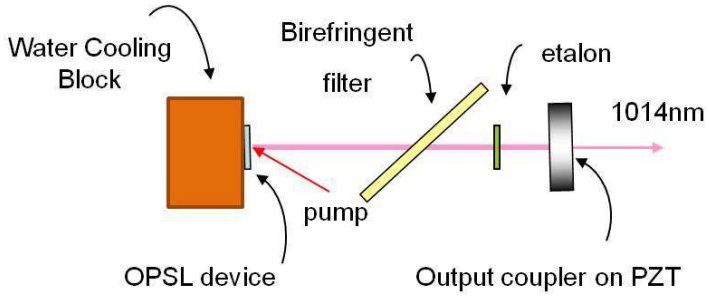

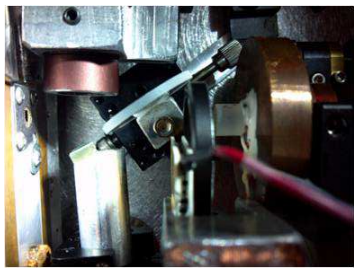

Figure 2.1: Schematic of OPSL, external cavity, and intra-cavity optics. External cavity is 7 cm long.

We use an 808 nm fiber-coupled diode laser to pump the OPSL. The pump spot is imaged onto the chip with a beam diameter of 200 µm. The interaction of the pump spot size with the resonator waist size has a strong effect on the lasing threshold, slope efficiency, and ability of the laser to operate single-mode. In general, it is best to maximize the amount of pumped surface area on the OPSL in order to achieve

high slope efficiencies. With this in mind, we designed the external cavity to have a mode size that matches the pumped area on the chip. The mode waist in our cavity is 125 µm. We took care to ensure the pump spot overlaps, but does not spill over, the resonator waist. If the pump waist exceeds the resonator waist, pump power will leak into higher-order cavity modes and inhibit single-mode operation.

The cavity is 7 cm in length and uses an output coupler with a 10 cm radius of curvature and 2% transmission coefficient. Our goal was to make the cavity as short as possible, while leaving room for the essential intra-cavity elements. A short cavity implies a large longitudinal mode spacing, which is desirable for single-mode operation. For frequency correction of the cavity resonance, the output coupler is mounted on a ring piezo and a donut-shaped copper mass. The copper mass helps increase the feedback loop bandwidth. The two additional intra-cavity elements, the birefringent filter and etalon, are incorporated to allow for precise tuning and suppression of multi-mode operation, respectively.

2.3 OPSL thermal properties

As noted in the previous section, temperature control of an OPSL device is critical. Our OPSL device absorbs nearly 60% of the incident pump light. If the power density on the chip approaches the thermal conduction rate of the heatsinking system, the power output of the OPSL will saturate and, as the power density exceeds this rate, will rapidly fall-off below the lasing threshold. This thermal rollover point, characteristic to all OPSL devices [49, 50], must be carefully considered when designing the cooling system.

The other major thermal consideration we considered was the temperature dependent wavelength of the chip. Ideally, when engineering the OPSL device, one should set the desired peak gain wavelength to coincide with an easily accessible temperature. In our case, since we were using surplus chips, we needed to set the temperature to 5 °C to achieve the desired power at 1015 nm. Operating the device at this low of a temperature increases the risk for condensation, which would damage the device. To mitigate the risk of condensation, we placed the OPSL and external cavity inside of a nitrogen-purged box. The chip itself was expertly bonded to a diamond substrate by Yushi Kaneda's group [47], which we then mounted onto the chiller heatsink using acetone and indium foil. This cooling arrangement allowed us to operate the device in a safe and efficient manner.

2.4 OPSL frequency properties

The OPSL lasing frequency can be adjusted using a combination of temperature and intra-cavity elements. OPSL gain bandwidths often span several nanometers; our specific chip spans about 14 nm. The temperature adjustment sensitivity is 1-2 nm for every 10 °C. At high pump intensities, the peak power can drop off significantly if attempting to force lasing off the gain peak.

The large gain bandwidth requires we pay particular attention to the cavity parameters in order to achieve single-mode operation on the TEM_{00} mode. To avoid multimode output into transverse cavity modes, we ensure the pump spot fills 90% of the cavity waist size. To avoid operation on more than one longitudinal mode, we minimized the cavity length, and employed the birefringent filter and etalon (see

Fig. 2.1) [45]. We set the cavity length at 7 cm, which allows just enough physical space for the other intra-cavity optics.

The first intra-cavity element, the Lyot filter, is a 2 mm thick birefringent plate mounted inside the cavity at Brewster's angle. By rotating the plate, a select band of wavelengths will be rotated back to the 'p' polarization state, and experience coherent buildup in the cavity. Other wavelengths will be rotated to varying degrees away from 'p' polarization and experience loss in the cavity. The second intra-cavity element is a 750 µm etalon. The etalon is a bandpass filter with a 200 GHz free spectral range. We mounted a peltier device onto the etalon to allow shifting of the etalon transmission peaks. Without this thermal adjustment capability, there would be inaccessible gaps of frequency space. This setup enables access to the cooling transition in all the common Hg isotopes. However, even with the intra-cavity elements, the OPSL laser would still experience mode-hops and brief periods of multi-mode operation. To eliminate these excursions from optimal performance, we mounted the OPSL and external cavity on a portable optical platform, and placed rubber dampening pads between the portable table and the air-suspension lab table. We placed a plastic box around the cavity to guard against air currents. All these steps, when fully implemented, allowed for indefinite stable frequency operation of the OPSL laser.

2.5 Second harmonic generation: generating the 507 nm intermediate frequency

Intra-cavity frequency doubling is a commonly used technique for efficiently generating higher harmonics [51]. The high intensities generated in an optical cavity significantly boost the efficiency of frequency conversion over that of a single-pass configuration. Although the cavity resonance must be actively locked, making the system sensitive to environmental perturbations, this disadvantage is offset by the high conversion efficiencies achievable. When designing the cavity, we must consider the ratio between beam waist and confocal parameter which yields optimal conversion efficiency. The importance of this ratio is outlined in detail in Boyd and Kleinmann [52]. In this section and the following section we describe the construction of the LBO and BBO cavities which generate the 253.7 nm cooling light in our system.

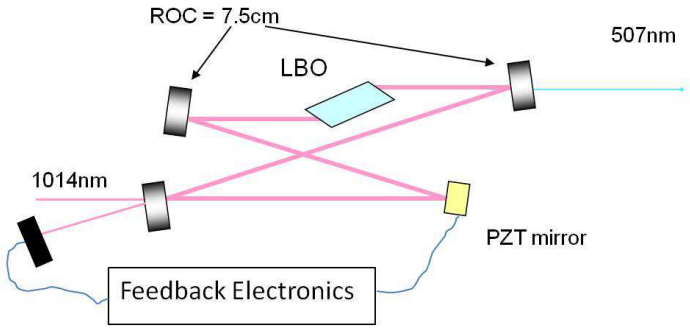

Figure 2.2: Bow-tie cavity configuration used to frequency double the OPSL wavelength to 507.5 nm.

The first intra-cavity stage utilizes an LBO (lithium niobate) crystal to generate 507.5 nm from the 1015 nm light originating from the OPSL. The cavity is con-

figured in a ring, or bow-tie, configuration (Fig. 2.2). Such a configuration allows for a compact foot-print and significantly reduces optical feedback into the OPSL. Despite this, we needed to insert an isolator after the OPSL to eliminate all feedback. The LBO crystal, which is Type I phase-matched, is 2 cm in length and both faces are cut at Brewster's angle. The phase matching of the crystal also exhibits some temperature dependance, so we attached a peltier device to the crystal mount along with a simple temperature feedback module. Although the Brewster cut faces introduce astigmatism to the beam profile, the cavity angle can be set such that the astigmatism from the cavity mirrors compensates this and results in a net zero astigmatism of the beam.

To lock the cavity on resonance, we glued a piezo onto one of the cavity mirrors and implemented a Hansch and Couillad locking scheme [53]. This method works very well in our case since the Brewster's cut crystal produces a sharp difference in cavity losses for 's' and 'p' polarization states. A custom circuit consisting of a birefringent Vanadate crystal glued to a double-balanced detector produces the derivative error signal used to lock to the cavity resonance. Testing of the feedback loop revealed a bandwidth of 27 kHz.

The output coupler mirror in the cavity is a dichroic designed to transmit greater than 95% of the generated 507 nm light. Figure 2.3 shows the power curve for all stages of the cooling laser. At 1287 mW of incident light, we measured 545 mW at 507 nm, yielding an efficiency of 42%. While our efficiency curve was below that of other experiments described in the literature [35, 47, 51], the power generated by our design was sufficient for our purposes. By nature of the LBO walk-off angle, the

green output exits the cavity with a 2:1 aspect ratio. We use a pair of cylindrical lenses to collimate the beam to a 1:1 profile. Since the beam is typically non-gaussian in the transverse direction, this is not a perfect solution and will result in sub-optimal coupling into the UV cavity.

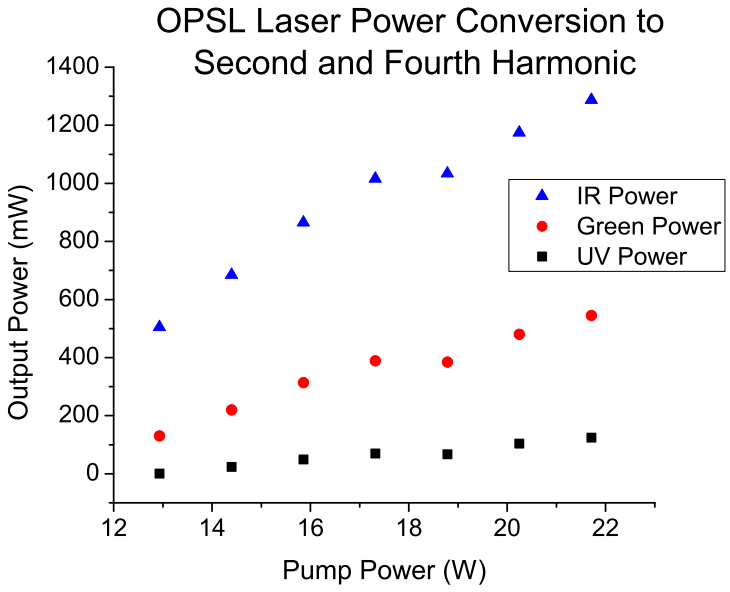

Figure 2.3: Power output for all stages of the OPSL relative to the OPSL pump laser power. At 1300 mW of IR, we achieved 42% conversion efficiency to the green and 9% conversion efficiency to the UV.

2.6 Fourth harmonic generation: generating the 253.7 nm cooling frequency

The next doubling stage produces the 253.7 nm cooling light. The cavity design, shown in Fig. 2.4, is very similar to the LBO cavity, with some notable exceptions. We use a 1 cm Type 1 phase-matched BBO (barium borate) crystal. The phase-matching of this BBO crystal has no sensitivity to temperature, but we still mounted

a peltier device to the crystal mount in order to hold the crystal temperature ∼5 °C above room temperature. Modest heating of the crystal protects against moisture damage, which can be particularly problematic for BBO crystals.

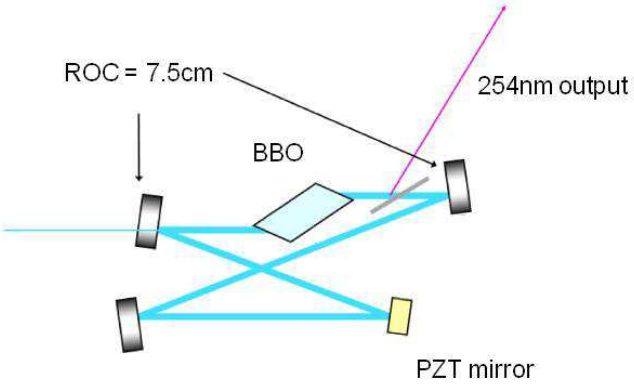

Figure 2.4: Doubling cavity for generating the 253.7 nm cooling laser light from the 507 nm intermediate stage. We use a BBO Type 1 phase-matched nonlinear crystal.

Another major difference with the BBO ring cavity lies in the method we use to couple out the fourth harmonic UV light. Previous experiments in the literature have noted the damaging properties of intense UV light as a significant source of power degradation [35, 54]. To avoid damaging an expensive dichroic output coupling mirror, we chose to use a Brewster plate to extract the generated UV from the cavity. The plate is transparent for the 'p' polarized fundamental (507 nm) and highly reflective for the 's' polarized UV.

Because the BBO crystal has a large walk-off angle, the UV beam profile exits the cavity with severe spatial distortion. This results in the beam having a guassian profile in one dimension, and a top-hat profile in the orthogonal dimension. Since we want a guassian profile for the MOT cooling beams, we constructed a filter to

clean the beam profile. We first collimate the guassian dimension using a cylindrical lens. Then we focus the beam using a 10 cm lens, which transforms the top-hat dimension into a sinc profile. The center lobe of a sinc profile closely approximates a guassian, and we can effectively filter that lobe using a horizontal slit placed at the lens focus. Figure 2.6 shows the output of the filter setup in the far-field, with the slit both open and closed. This filter setup transmits 90% of the UV optical power emerging from the cavity. After the filter, the UV light propagates to the saturated absorption setup and the MOT chamber.

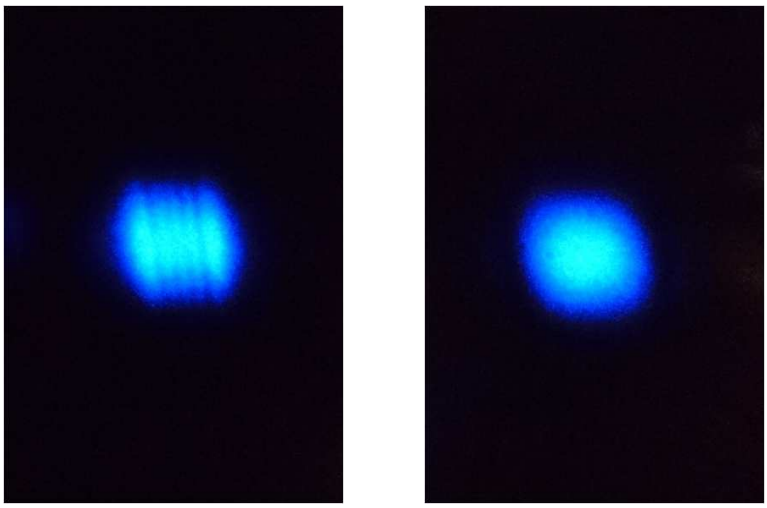

(a) (b)

Figure 2.5: (a) UV cavity output with no spatial filter. (b) UV cavity output with a spatial filter.

2.7 Stabilization of the OPSL laser system

A stable magneto-optical trap requires that the linewidth of the cooling laser be less than the cooling transition linewidth. We must also be able to detune and lock

the cooling laser several megahertz below the cooling transition peak. A heterodyne measurement revealed a 300 kHz free-running linewidth for the OPSL laser, which corresponds to a linewidth of 1.2 MHz in the UV. To push the linewidth well below this point, we needed to stabilize the OPSL laser to an external reference. One possibility would be to lock the OPSL cavity directly to the cooling transition. However, since the locking spectroscopy would occur in the UV, both doubling stages would need to follow any fast corrections to the OPSL. Since we expected the OPSL to have a much higher bandwidth than the doubling cavities, this was a less than optimal solution. In the most likely scenario, the doubling stages would unlock everytime the OPSL lock was activated. To avoid this situation, we employed a passive zero-dur reference cavity as an intermediary in the transition locking setup. The OPSL would be directly locked to the zero-dur cavity for absolute linewidth narrowing, which effectively bypasses the doubling stages. Then, the zero-dur cavity would be locked to the cooling transition using a slow adiabatic feedback loop. With this method, we are not limited by the slower response of the doubling stages.

The OPSL is stabilized to the 1 MHz linewidth zero-dur cavity using a side-of-fringe lock. We chose a side-of-fringe lock for its simplicity of implementation compared to an FM lock. The cavity is 10 cm long and uses two 30 cm radius-of-curvature end mirrors. A small amount of 1015 nm light from the OPSL is directed to this cavity. The error signal generated by this cavity is then fed to a PI^2 controller, which drives the piezo mounted to the OPSL cavity output coupler. After locking the OPSL to this reference cavity, we characterized the linewidth by heterodyning the stabilized OPSL light with a diode laser. The linewidth of the diode laser was

$\sim$20 kHz. We measured the instantaneous beatnote linewidth, which provided us with an upper bound value of 70 kHz for the stabilized OPSL linewidth. After boosting the OPSL piezo feedback bandwidth from 3 kHz to 30 kHz, we measured an OPSL linewidth near 10 kHz, which corresponds well with other measurements from the literature [44–46].

To create an offset lock to the 6^1S_0 - 6^3P_1 cooling transition, we split a small percentage of the cleaned UV output and direct it through two sequential AOMs. The AOMs are driven in a differential manner to blue-shift the beam 0-6 MHz. This effectively red-shifts the MOT beams by the same amount. After propagating through the AOMs, this weak beam enters a saturated absorption spectroscopy setup, where the pump/probe interact inside a 1 mm thick mercury vapor cell. Using this setup, we resolved the following mercury isotopes: ^{198}Hg, ^{199}Hg, ^{200}Hg, ^{201}Hg, ^{202}Hg, and ^{204}Hg. While ^{196}Hg is also a naturally occurring isotope, its abundance is very low (0.15%), and we were unable to resolve it. The frequency spacings of the cooling transition for the various isotopes have been mapped out in the literature by F. Bitter and Scheid et. al. [35, 55]. In this section we present details for spectroscopy of the cooling line in ^{200}Hg, since the large abundance of this isotope yields high SNR measurements.

To scan and resolve the ^{200}Hg line, we activate all the system locks, including the OPSL lock to the zero-dur cavity and the doubling cavity polarization locks. We then apply a slow scan voltage ($\sim$ 10-30 Hz) to the reference cavity, all the while monitoring the Doppler-free probe beam in the saturated absorption setup. Figure 2.6a shows a Doppler-free scan of the cooling line, revealing a FWHM of 1 GHz.

Zooming in on the scan (Fig. 2.6b), we measure a linewidth of 4 MHz. To lock to the transition, we apply a 100 kHz modulation signal to one of the AOM drivers, and use a lock-in amplifier to generate a derivative error signal from the saturated absorption peak (Fig. 2.7a). We then feed this error signal to a PI servo, which applies a slow correction to the reference cavity in order to keep the OPSL on the cooling transition.

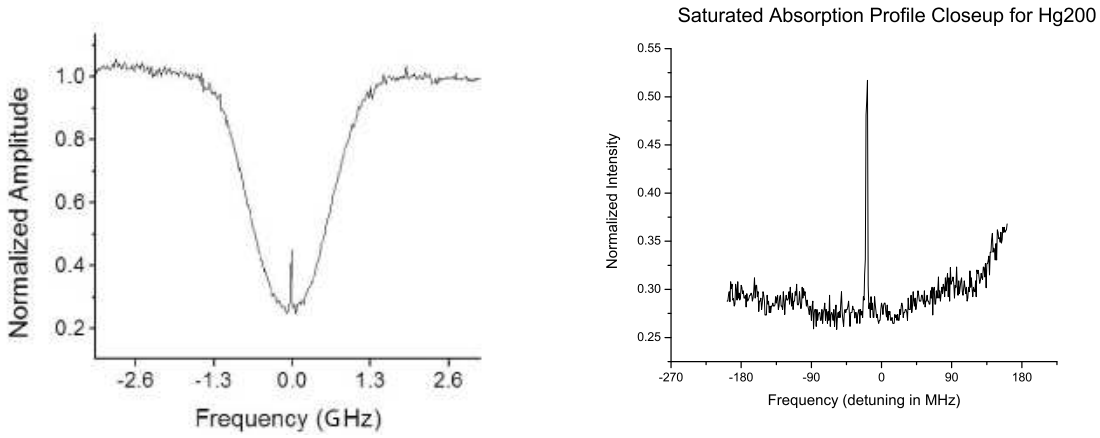

(a) (b)

Figure 2.6: (a) Doppler-scan of ^{200}Hg. (b) Zoom-in of the Doppler-free peak. The FWHM linewidth is 4 MHz.

Using the derivative error signal as a reference standard, we calibrated the drift of the zero-dur reference cavity. In Fig. 2.7b, we plot the frequency drift of the cavity relative to the cooling transition. The data in this plot corresponds to an Invar cavity that was briefly used to stabilize the OPSL, prior to being swapped out for the zero-dur cavity. The drift rate shown is about 1 MHz/sec, but this dropped to 1 MHz/min for the zero-dur cavity. We also characterized the UV linewidth by measuring the RMS voltage of the error signal while the reference cavity was locked

to the cooling transition. Figure 2.7c shows a linewidth of approximately 320 kHz, which is well below the 1.27 MHz natural linewidth of the transition.

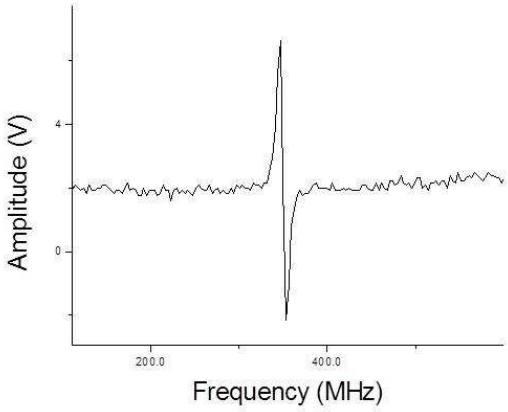

(a)

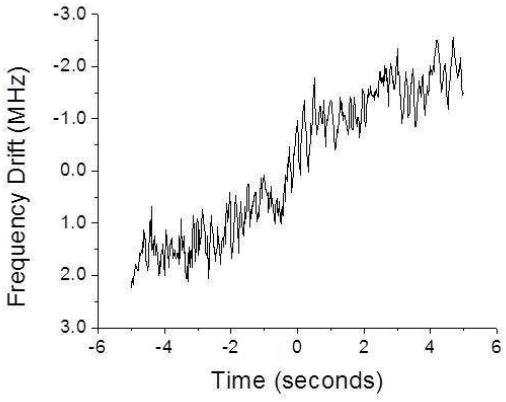

(b)

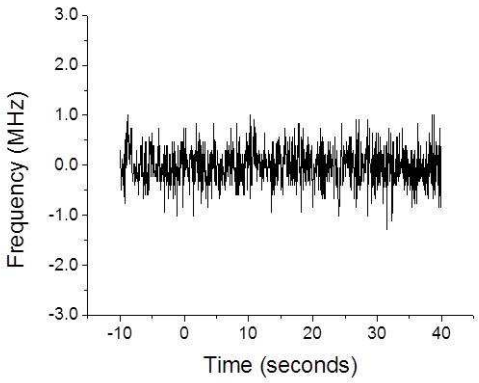

(c)

Figure 2.7: (a) Error signal generated from the Hg saturated absoprtion peak. (b) Drift rate of the Invar reference cavity originally used to stabilize the OPSL. (c) RMS voltage of the saturated absorption error signal while OPSL is locked to the reference cavity, showing 320 kHz linewidth (UV)

The experimental setup described in this chapter was the first demonstration applying OPSL technology to precision spectroscopy in the deep ultraviolet. The

system served as an excellent platform for demonstrating a mercury MOT and detecting the Hg clock transition [37]. Although we ultimately had to replace the OPSL source for reasons beyond our control (see Chap. 3), we have shown that OPSL lasers remain a viable choice for atomic spectroscopy applications.

CHAPTER 3

Replacement MOT source: ytterbium fiber amplifier at 1015 nm

3.1 Advantages to replacing the OPSL Source

Our original MOT trapping laser, the OPSL described in Chap. 2, demonstrated overall excellent properties for cooling and trapping neutral mercury. However, in the eventuality that the OPSL chip failed, we did not have a reliable method for sourcing a new chip. Upon experiencing some power issues with the OPSL device, we chose to replace the system. We tested several new VECSEL chips in the laser cavity, but none of these chips could be operated successfully at 1015 nm. Lacking internal capability to produce the VECSEL chips, we embarked on a project to replace the OPSL cavity. We set out to build a fiber-amplified ECLD system [56–58] as a replacement for the OPSL source. In this section I describe the process we used to construct and test a fiber amplified ECLD at 1015 nm.

3.2 Background and basic theory of Yb-doped fiber amplifiers

Fiber amplifiers are frequently desired for medium to high-power laser applications. With inherently low pump thresholds and high slope efficiencies, they possess higher gain and better spatial mode quality than most tapered amplifiers. The introduction of double-clad fibers (DCF) paved the way for the development of very high power multi-kilowatt fiber lasers and amplifiers [59, 60]. One major limitation of

fiber amplifiers is their limited tunability. Both erbium and ytterbium systems are constrained to relatively narrow regions of the spectrum. Ytterbium-doped gain fiber is highly valued for its optimal performance near 1064 nm, but exhibits faults when deviating more than $\pm \sim$10 nanometers from this point. Below 1064 nm, the absorption of ytterbium rises [61], resulting in increasing levels of amplified spontaneous emission (ASE) at these shorter wavelengths. ASE will effectively steal gain from the amplified signal mode, limiting the gain at the signal wavelength and causing potentially damaging levels of ASE in the fiber. If ASE levels can be suppressed to levels below the damage-threshold of the doped-gain fiber, the excess ASE at the output can be easily filtered. The main concern is to minimize the effect of the ASE on the signal gain.

Ytterbium amplifiers have been effectively modeled at many different pump and signal wavelength configurations. The rate equation model used for ytterbium is nearly identical to that of erbium [62], with simplifications arising from the more basic level structure of the Yb^{3+} doping ion. Extensive studies of the absorption and emission profiles of Yb fiber have been carried out [61]. Yb-doped gain fiber acts like a quasi 3-level system at the shorter wavelengths where absorption is higher. Predictably, seeding a Yb amplifier with signal light at 1015 nm will result in an ideal environment for the accumulation of forward and backward propagating ASE. This ASE will have a back-action on the excited state population [61, 63–65], resulting in a negative effect on the signal gain in the peak gain range of 30-40 dB.

Initial successful attempts to side-step the ASE problem below 1064 nm centered around cryogenic conditioning of the doped gain fiber. A few cases in the literature

demonstrate amplifiers where the Yb-doped fiber is immersed in liquid nitrogen, which depopulates the ground states, reducing absorption and effectively shifting the absorption curve [66, 67]. In Steinborn et. al. [67], they demonstrate a 10-W amplifier at 1015-nm consisting of 7-m of doped gain fiber immersed in a 77-K nitrogen bath. The ASE is suppressed by 20-dB below the signal at 25-W of pump power. Despite these positive results, LN_2 treatment is a costly and time-intensive proposition.

Because of the logistical problems inherent to a liquid nitrogen solution, Hu et. al. [57, 58] proposed and tested an alternate method for a Yb-doped amplifier at 1015 nm. Based on the reasonable assumption that Yb-doped fibers are dominantly homogeneously-broadened at room temperature, we can express the gain at 1015 nm in terms of the gain at two other wavelengths:

$$G_{1015} = \frac{G_{1035}}{1.13} - 0.0375\frac{A_{clad}}{A_{core}}\alpha_p. \tag{3.1}$$

We chose G_{1035} since the peak ASE gain will occur at 1035 nm. The other independent gain variable, α_p, represents the negative gain (absorption) at the 976 nm pump wavelength. By inspection of Eq. 3.1, we see that maximizing the gain at the signal wavelength (1035 nm) can be achieved by reducing the cladding-to-core ratio (A_{clad}/A_{core}) and reducing the absorption at the pump wavelength. A decrease in absorption is most easily effected by shortening the length of the Yb-doped fiber. On the flip-side, shorter gain fiber will cause a drop in efficiency, but this can be compensated with additional pump power. Given the wide availability of low-cost

fiber-coupled pump diodes, adding pump power is an inexpensive and simple option. Figure 3.1 shows the increasing ASE relative to pump power in a 40 cm section of gain fiber.

Hu et. al. [57] report 8 W of power at 1015 nm using 45 W pump power at 976 nm. They demonstrated these results using slightly more than one meter of Yb-doped DCF. In rest of this section, I describe our implementation of a similar type of amplifier. This amplifier replaced the now defunct OPSL source and currently serves as the mercury cooling and trapping laser.

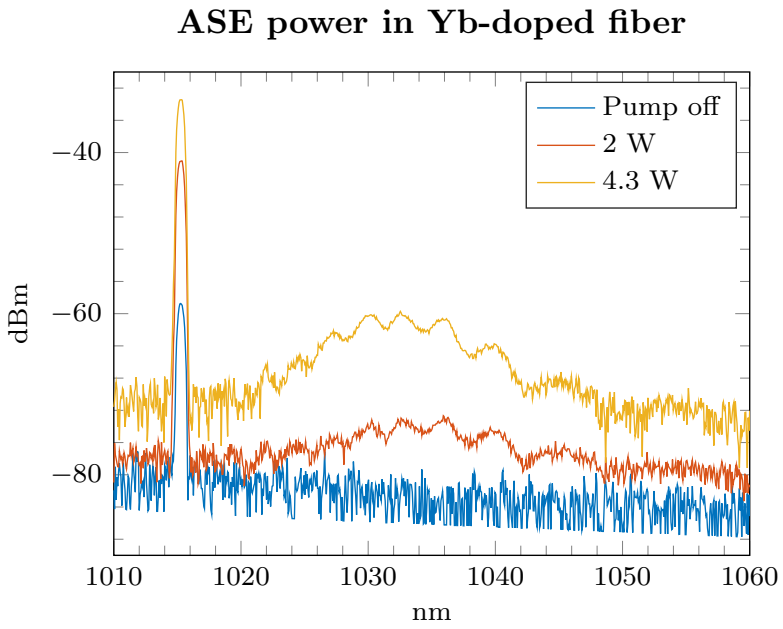

Figure 3.1: Rise in ASE in a 40 cm section of gain fiber with a 976 nm pump

3.3 Amplifier requirements and design

The OPSL system yielded 1.5 W of single-mode power at 1015 nm, which was sufficient to demonstrate and run our Hg MOT on a consistent basis. As a prerequisite, any suitable replacement of the OPSL should also be able to generate 1.5 W of single-mode power. The 6^1S_0 - 6^3P_1 intercombination cooling transition has a 1.3 MHz linewidth. The OPSL system has a stabilized linewidth near 10 kHz, yielding 40 kHz FWHM in the UV. The ECLD source for the new system (Toptica DL-Pro) has a free-running linewidth of 100 kHz in the IR (400 kHz UV), still well below the transition width. With stabilization of the ECLD, we expect the linewidth to drop even further. We were not concerned about any linewidth problems with the new source; our main concern was to generate sufficient power.

Figure 3.2 shows the layout of the cooling laser system. As noted above, we used a Toptica DL-Pro ECLD for the amplifier seed source. At 1015 nm, the Toptica produces 30 mW of single-mode power. Initial tests showed we could couple light into the DCF (Double-Clad Fiber) with 60% efficiency. Accounting for all optical losses, we could reasonably inject 15mW-17mW of seed light into the gain fiber. Given the absorption of the gain fiber at 1015 nm, we decided to add an extra margin of safety against ASE by building a pre-amplifier. The pre-amplifier would seed the main amplifier with 150 - 200 mW, well in excess of the 31 mW saturation level of the Yb-doped gain fiber. Because we did not have a fiber-coupled optical isolator at our disposal, the two stages would be coupled together using a section of free-space optics.

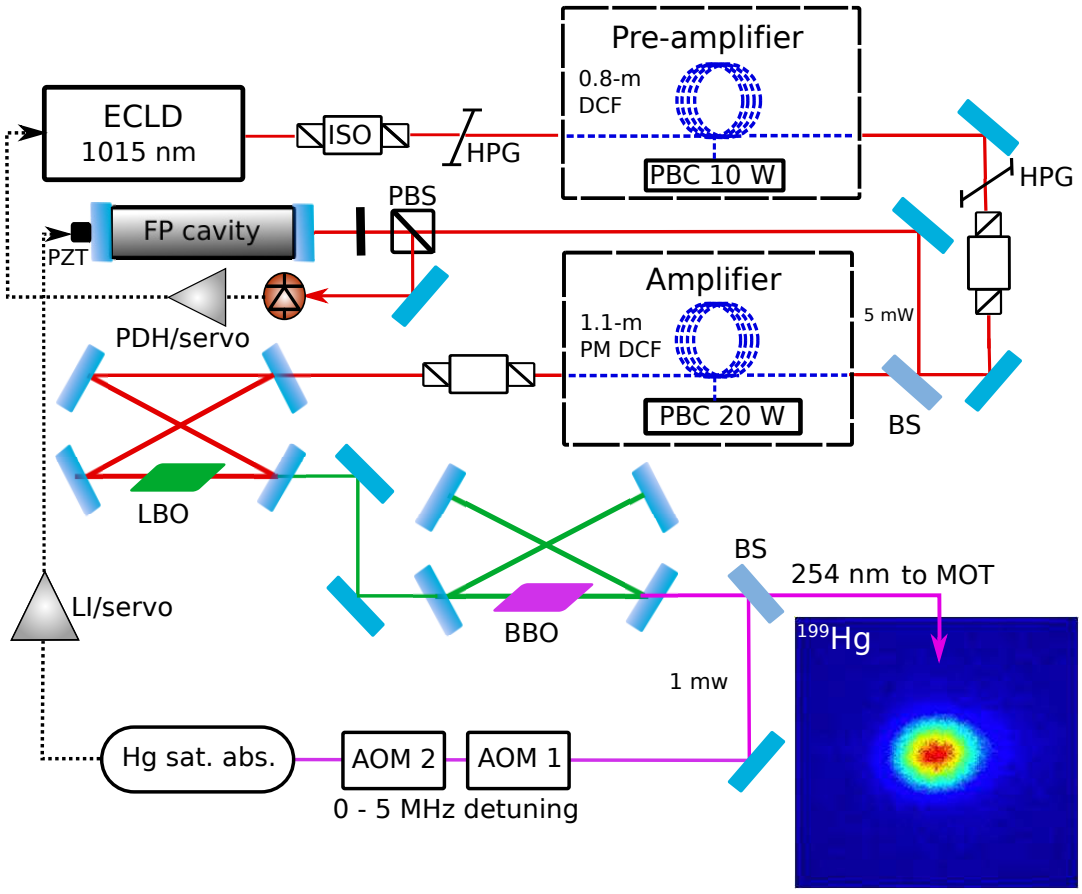

Figure 3.2: Layout of the cooling laser system. ISO: isolator; DCF: double-clad fiber; BS: beam-splitter; LI: lock-in; PDH: Pound-Drever-Hall; PBC: pump beam combiner; HPG: high-power grating; PM: polarization-maintaining.

3.4 Pre-amplifier stage

During construction of the pre-amplifier stage, we took the opportunity to test the response of the signal power and ASE power at different pump wavelengths. The analysis in Sec. 3.2 assumes a pump wavelength of 976 nm, but a 915 nm pump will result in a different ASE profile. The 915 nm pump will generate higher levels of ASE than a 976 nm pump, since broad spectrum emission centered at 976 nm will

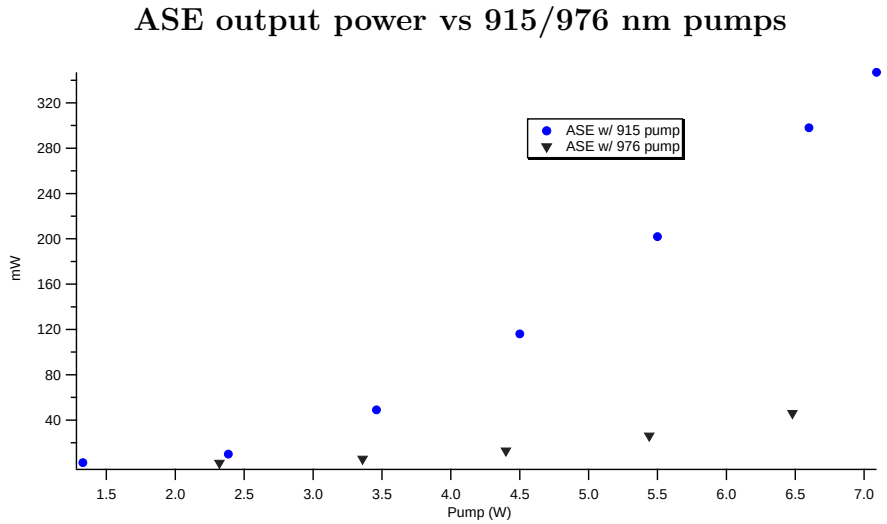

Figure 3.3: ASE power is significantly greater with a 915 nm pump due to the large emission cross-section at 976 nm. This test used 40 cm of 10/125 µm Yb-doped gain fiber.

be present in the absence of 976 nm pump light [61]. Figure 3.3 shows, as predicted, significantly greater ASE generation with the 915 nm pump.

To construct the pre-amplifier stage, we first collimate and isolate (45 dB) the ECLD output. As an added precaution against damage to the ECLD from back ASE, we insert a high-power diffraction grating immediately prior to the fiber coupling optics.

The coupling stage uses a 4.3 mm focal length asphere to seed light into a section of passive fiber spliced to a standard pump beam combiner. A 10 W pump diode is spliced to the pump fiber lead of the pump beam combiner. The pre-amplifier uses DCF non-PM fiber (NUFERN PLMA-YDF-10/125-VIII). We chose non-PM fiber primarily because it was readily available, and we were confident in our ability to suppress polarization drifting in an amplifier with a very short gain section. The

input fiber end was angle cleaved for protection of the ECLD from feedback and protection of the amplifier from self-induced oscillation of ASE.

In addition to the pump wavelength comparison test (Fig. 3.3), we tested the pre-amplifier with 80 cm of Yb-doped DCF gain fiber. Figure 3.4 demonstrates our ability to generate several hundred milliwatts of signal power (1015 nm). During the tests referenced in Figure 3.4, the pump diode was held at 10 °C. After performing a test with the pump at 21 °C, the power efficiency increased, and we measured 550 mW of power at 7 W of pump power. We expect high sensitivity of the gain to pump temperature given the relatively narrow absorption feature of ytterbium at 976 nm.

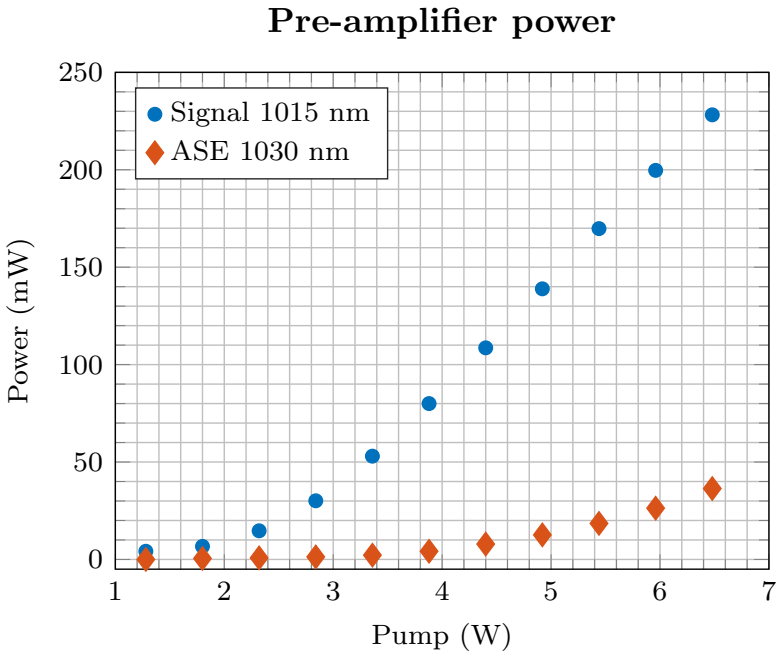

Figure 3.4: Pre-amplifier output power with 17 mW of seed and 80 cm of Yb-doped gain fiber. Pump temperature was a constant 10 °C during this test. Additional testing with the pump temperature at 21 °C yielded 550 mW at 7W of pump power.

As noted earlier, the pre-amplifier stage uses non-PM (polarization maintaining fiber). We ensure polarization stability by protecting the fiber from environmental noise and inserting a stress plate near the end of the gain fiber. Next, we couple the output of the pre-amplifier into free-space through the bare fiber, angle-cleaved facet. The beam is then collimated with a 2 cm fused-silica aspheric lens. Since we are not using a connectorized output and a packaged collimator, alignment of the output facet and lens is critical. The combination of angle-cleaved output and fast collimating lens requires sensitive alignment in order to avoid severe astigmatism of the output beam profile. The VECSEL system had a high-quality spatial profile and we wished to preserve that excellent profile with the fiber amplifier. The downstream LBO ring cavity was configured to reduce astigmatism generated by the folded optical path, but this was dependent on a zero-order guassian spatial input mode. To effectively collimate the amplifier output, we use an adjustable focus chuck mount for the fiber and a 3-axis mount for the lens. Then, after mounting a CCD in the far-field, we image the beam onto the CCD and adjust the fiber chuck and lens mount iteratively until visual inspection yields $M^2 \approx 1$, both inside and outside of the far-field focal point.

The collimated beam propagates through a high-power transmission grating and faraday isolator, after which approximately 1% of the beam power is diverted into a 10 cm Fabry-Perot cavity. This cavity serves to stabilize the drift and narrow the linewidth of the seed ECLD. The cavity lock uses the PDH method, where the FM modulation is provided by modulating the ECLD current at 12.5 MHz. The remainder of the pre-amplifier power seeds the main amplifier stage. We do not

measure any significant drift in the pre-amplifier output polarization despite the use of non-PM fiber. In our experience, only slight adjustments to the stress-plate every few months were required in order to compensate for any polarization drift.

3.5 ECLD frequency stability control

To stabilize the ECLD frequency, and provide a method for frequency offset locking to the mercury cooling line, 6^1S_0 - 6^3P_1, we implemented a PDH lock to a passive reference cavity. The cavity consists of a 10 cm zero-dur spacer, a Noliac-brand ring piezo, and two 30 cm radius-of-curvature mirrors bonded to each end. We measured a 1 MHz linewidth for the cavity. This cavity originally served to stabilize the OPSL laser cavity (Chap. 2). As shown in Fig 3.2, the ECLD is locked to the zero-dur cavity, which itself is locked to the Hg saturated absorption cooling line. Approximately 1% of the light from the pre-amplifier stage is diverted for the reference cavity lock. The Hg saturated absorption setup is described in detail in Chap. 2. The error signal for locking the ECLD to the cavity is provided by modulating the ECLD current at 12.5 MHz. Mixing and demodulation of the error signal is performed using a Toptica Digilock digital feedback control system.

3.6 Amplifier stage

We seed the amplifier stage with 500-600 mW of incident power which translates to $\sim$160 mW in the fiber. Since the amplifier stage uses PM fiber (NUFERN LMA-YDF-10/125-VIII), we inserted a half-waveplate at the input to set the polarization. The coupling lens is a 6.5 mm asphere. The amplifier stage is pumped with two

10 W pump diodes at 976 nm. To determine the optimal gain fiber length for the stage, we tested a selection of gain fiber lengths from 1 - 1.5 m, measuring the signal and ASE power for each length. Figure 3.5 shows the results of these tests. The well-defined increase in ASE power at 1.2 m delineates a turnover point where the ASE power begins to clamp the signal gain. Extending the gain fiber length beyond 1.2 m would clearly be detrimental to the system performance, so we selected 1.1 m for the length of the amplifier stage.

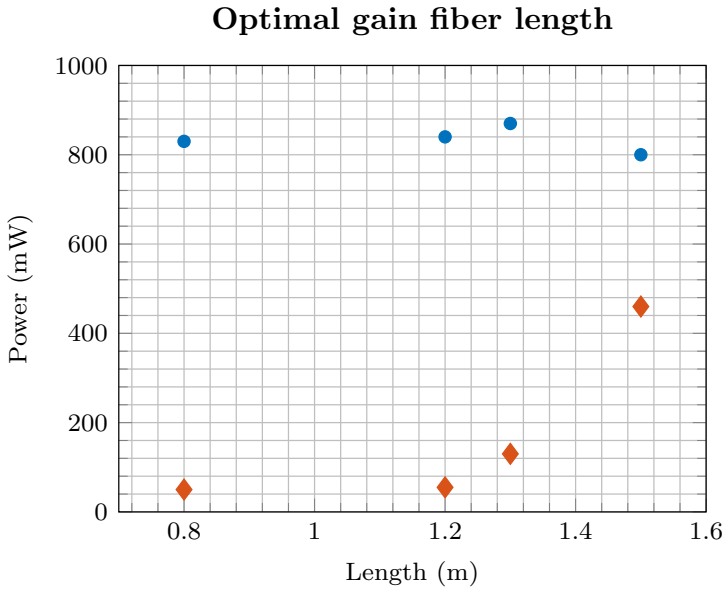

Figure 3.5: Plot showing the turnover point as ASE power begins to draw power out of the signal mode. Blue dots represent signal power; orange dots represent total power (ASE + signal).

While testing the power in the second stage, we observed a gradual drift in the output polarization. This drift would occur characteristically over a period of 2-4 hours, causing the power, measured through an isolator, to change by 30 - 50%. Working our way through the amplifier, we verified the stability of the polarization

in each section. After the tests, we suspected the issue might be the result of a mismatch between the inner cladding diameter of the pump beam combiner and the inner cladding diameter of the gain fiber. After replacing the pump beam combiner, the problem resolved itself. We are unsure of a physical explanation for this drift phenomena.

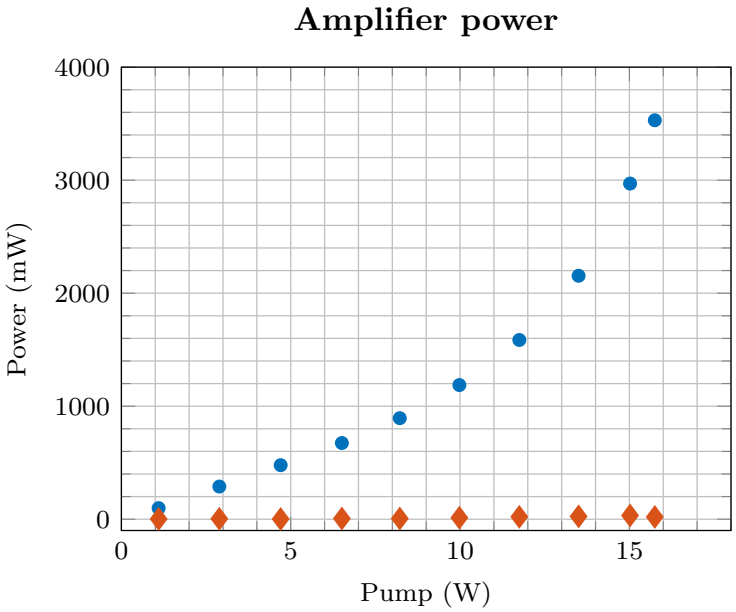

Figure 3.6: Amplifier output power. Blue dots represent signal power; orange dots represent ASE power

The output of the amplifier stage is collimated with a 2.5 cm fused silica lens. We do not insert a grating at the output, since the downstream doubling cavities will filter any broadband ASE. The amplifier stage is capable of producing up to 3.5 W at 1015 nm (Fig. 3.6). The high seed level and short section of gain fiber allows for strong suppression of the ASE, mitigating any concerns of fiber damage or broadband noise in the output.

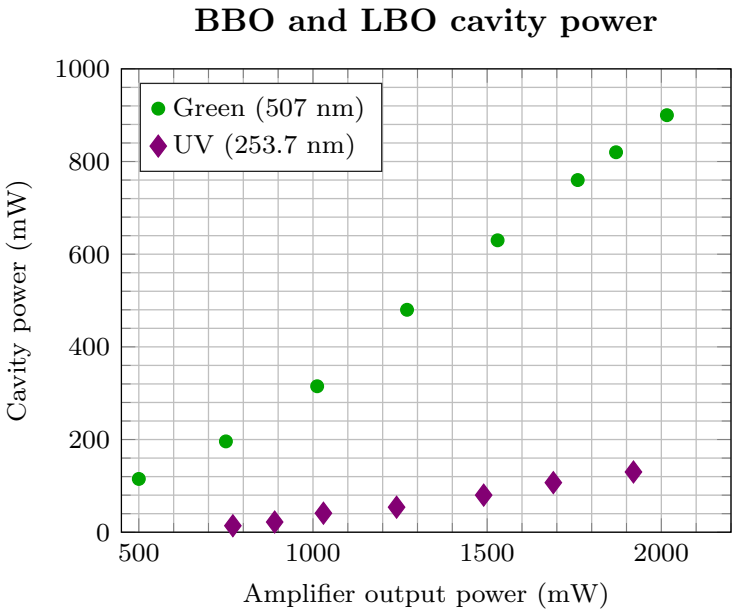

Figure 3.7: Cavity output power relative to amplifier power at 1015 nm.

After successfully demonstrating the amplifier operation, we collimated the output beam profile using the same procedure described for the pre-amplifier stage, taking care to avoid astigmatism. After passing through an optical isolator, the amplifier light is coupled into the LBO doubling cavity. Details of the doubling cavities can be found in Chap. 2. We made no major adjustments to the doubling cavities after integrating the fiber amplifier light. Measuring the power after the LBO and BBO stages, we demonstrate the ability to generate powers on the same order as the OPSL system (Fig. 3.7) Because of the strong ASE suppression in the amplifier stage (Fig 3.6), we predict the amplifier can be scaled to produce as much as 7 W at 1015 nm, simply by adding additional pump power. Operating at higher powers would require additional components to protect the fiber output, but would prime the system to generate several hundred milliwatts of cooling light at 253.7 nm. With

appropriate measures taken to mitigate UV damage, higher power UV cooling light would boost atom numbers and atom densities inside the MOT, which could significantly improve the long-term fractional frequency stability of lattice-based mercury optical clocks. Because of the reliability and scalability unique to fiber-amplified ECLD systems, we believe our system to be a superior choice to other mercury cooling laser sources, such as tapered amplifiers and Yb:YAG disc lasers.

CHAPTER 4

Construction of the mercury MOT apparatus

The experimental apparatus required for a mercury magneto-optical trap mirrors that of many other alkaline-earth MOT systems. In addition to the cooling laser, described in Chapters 2 and 3, we require a vacuum system and magnetic field coils. The vacuum system design must allow proper optical access for the cooling wavelength, and provide a method for controlling flow of the atomic species into the chamber. For the coils, we must consider current and cooling requirements. In this chapter, we describe the specifications and construction of the mercury MOT apparatus.

4.1 Main chamber and MOT optics

For the main vacuum chamber (Fig. 4.1), we use a stainless steel chamber with six 1.75" horizontal window ports and two 6" vertical window ports. We use six of the eight ports for optical access, and these ports are equipped with custom AR-coated UV-grade fused silica ports. The custom windows are mated to the ports using a special technique designed to prevent uneven pressure across the window [68]. The vacuum hardware, being designed for ultra-high vacuum, uses Conflat flanges. The chamber is pumped with two Duniway Corp. ion pumps, a 30 L/s and a 50 L/s unit. The pumps are placed at opposite end of the chamber to create a differential

pumping layout. Differential pumping allows for future implementation of an atomic beam.

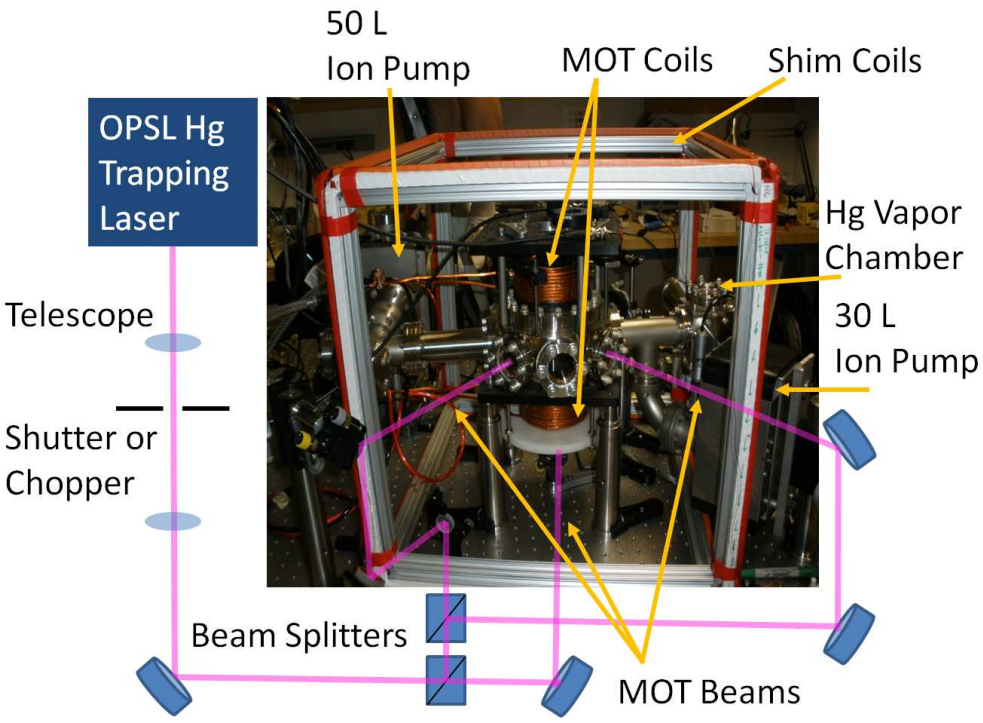

Figure 4.1: MOT system layout, including vacuum chamber and optics. OPSL source (top left corner) was later replaced with the fiber-amplified ECLD described in Chap. 3.

The chamber was prepared for use by properly washing all vacuum-exposed components and performing a bake-out on the chamber for over a week. We set the bake-out temperature near 180 °C, and used temperature sensors to ensure the windows never exceeded 200 °C. Despite our precautions with the windows, several windows exhibited stress-induced birefringence and had to be replaced. In hindsight, we should have done the original chamber bake-out with blanks covering the window ports. The replacement windows caused no issues with maintaining the

chamber pressure near our target value of 10^{-9} torr.

For transferring the 253.7 nm light from the cooling laser to the chamber, we expand the beam diameter to 15 mm. We then use a combination of polarizing beamsplitters and $\lambda/2$ waveplates to equally divide the power into three beams. Finally the beams are sent into the chamber such that they intersect orthogonally in the center of the chamber. We install $\lambda/4$ waveplates to implement a traditional $\sigma+$ / $\sigma-$ optical trapping configuration [69].

4.2 Secondary mercury source chamber

The high vapor pressure of mercury provides a substantial benefit over several other optical clock species: it eliminates the need for an oven to fill the chamber with vapor. Other species, such as ytterbium and strontium, must be heated to several hundred degrees celsius and formed into a thermal beam in order to load the MOT. This oven contributes to blackbody radiation, an undesirable contributor of noise to the clock state. Instead, we can store the mercury near its freezing point (-40 °C) when no vapor is required, and allow the temperature to rise by 10-30 °C in order to load a MOT. In our case, the MOT is loaded directly from the background vapor, but Petersen et. al. [32] have also demonstrated a MOT loaded by a non-thermal mercury beam. This would be beneficial for loading a lattice, a process generally requiring very low background vapor pressures.

The chamber we use for generating the background vapor consists of a simple cube vacuum chamber with 6 conflat ports. One port is for mating the entire system to a turbopump, one port is a standard viewport for visually inspecting the

Hg source, one port is blanked, one port mates to the main chamber, one port serves as an electrical feedthrough for controlling a peltier cooler and a temperature sensor, and the final port holds the peltier heatsink.

We designed the heatsink to be able to maintain the Hg temperature as low as -70 °C. The heatsink is a large cylindrical mass of OFHC copper with an inner channel machined for water flow (Fig. 4.2). The top surface of the heatsink mates directly to the conflat port knife edge, in precisely the same manner as a copper gasket would. The portion of the top heatsink surface exposed to the vacuum provides a platform to support the peltier cooler and Hg containment bowl. The original peltier cooler failed in the Fall of 2014, at which point we replaced the heatsink with a newly machined model of similar design, but with smaller dimensions and overall lower mass. While the original heatsink was salvageable, it was heavily contaminated with mercury residue, and for safety reasons, we chose to discard it and build a new one.

The original peltier cooler was a two stage unit from Marlow Industries (NL2064). We bonded the peltier to the heatsink using EPO-TEK H72, a low out-gassing, thermally conductive epoxy. On top of the peltier, we bonded a small OFHC copper bowl, just large enough to contain a few drops of mercury, but not so large as to place a significant thermal load on the peltier. The current leads of the peltier were soldered to an electrical feedthrough conflat. At this time we did not have a temperature sensor installed, and hence were unable to verify the peltier current-temperature performance curves. We simply relied on our ability to reduce the chamber pressure below 10^{-9} with the device current near its maximum value. Figure

4.2 shows the mercury source setup when assembled and installed in the chamber.

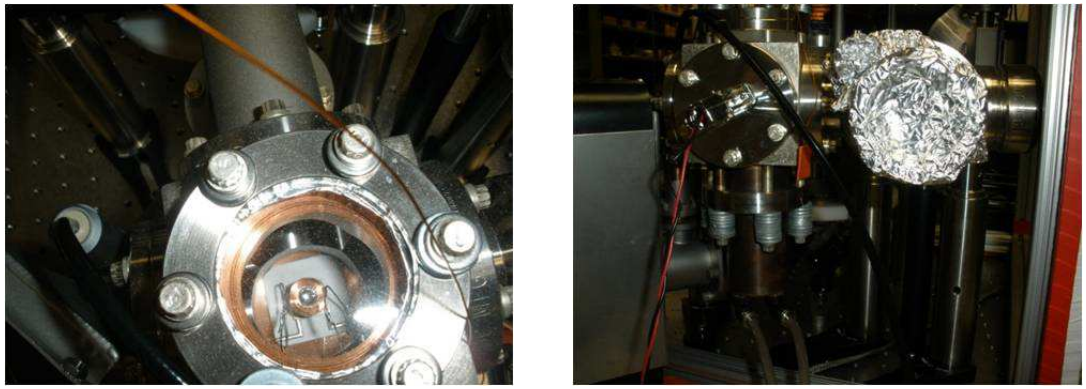

(a) (b)

Figure 4.2: (a) Mercury vapor source. (b) Vapor chamber attached to main chamber.

As mentioned earlier, the Marlow Industries device failed (broken lead), so we replaced it with a Custom Thermoelectrics 04812-5L31-04CFG peltier unit. This is a 2-stage device with a maximum temperature differential (ΔT) of 83 °C. The new unit was mounted and bonded using the same methods as described for the old device. When we installed this unit, we also mounted a thermocouple probe (OMEGA FF-K-24-25) to the side of the copper bowl, and wired the leads through the feedthrough.

Using the Custom Thermoelectrics unit, we found that we could reduce the temperature of the mercury containment bowl to a minimum of -50 °C. We set the peltier current to 3.35 A / 3.7 V to achieve this temperature. At this temperature, the mercury is frozen, and the chamber pressure reads 0.7e-9 Torr on the 50 L pump and 0.9e-9 Torr on the 30 L pump. Pumping down from atmosphere, the system should reach these pressure values in about 24 hours.

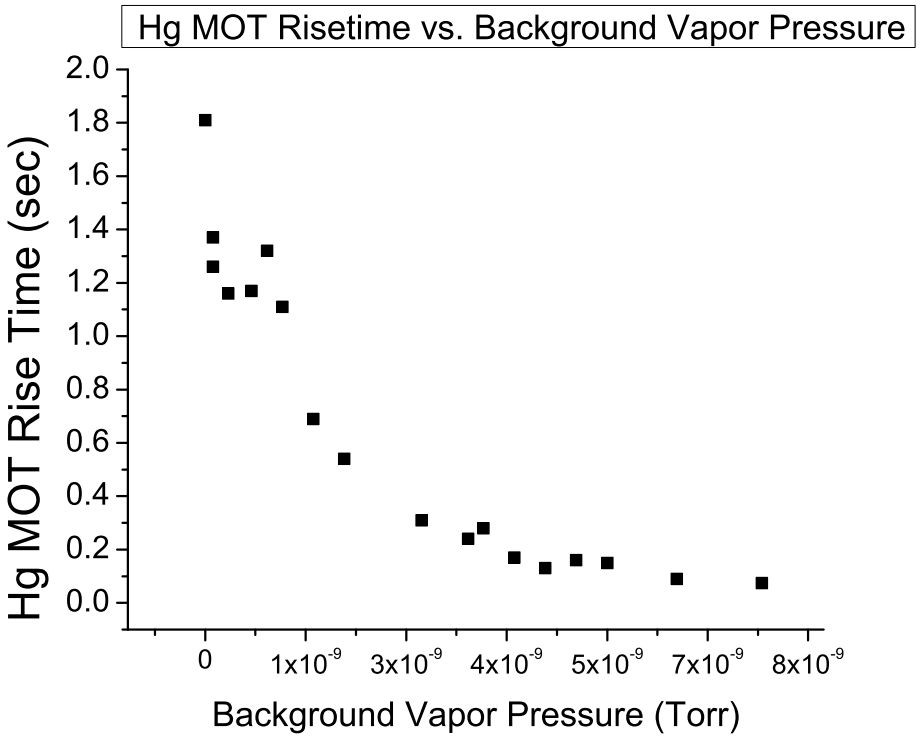

Figure 4.3: Rise time of the neutral Hg MOT

Once we had achieved a stable MOT, we measured the rise time of the MOT relative to the background vapor pressure. Background pressure has a strong effect on the MOT dynamics, as a higher pressure will result in a higher collision rate, causing atoms to cycle through the MOT more quickly. The rise time also has important ramifications for precision spectroscopy of the clock transition. Figure 4.3 shows the results for the rise time measurements.

4.3 Magnetic field construction and characterization

The red-detuned laser cooling beams will only form an optical molasses. To form a trap, we must also generate a magnetic field gradient at the intersection point of the cooling beams. When a gradient magnetic field is applied to a molasses, each atom will be continually shifted into resonance with the cooling beams. Atoms entering the beam intersection region with a slow enough velocity will then be trapped near the zero-point of the field gradient.

We use a pair of coils in an anti-Helmholtz configuration to generate the field gradient. For our coils, we chose to use kapton-coated hollow-core copper wire. The hollow-core allows for water cooling directly inside the coils. The wire has a square profile with an inside/outside diameter of 2.25/4.45 mm. The coils are mounted on 6" reducer flanges on the top and bottom surfaces of the main vacuum chamber. The coils fit snugly around the 2.75" window ports used for the vertical cooling beam. We use a 50 A Agilent current supply to power the coils.

In the literature, Petersen et. al. [70] estimated that a 15 guass/cm field gradient is necessary for trapping and cooling mercury. To calculate the gradient, we need to know the axial and radial components of the B-field. The axial component at a distance z from a single coil of radius R and current I is given by

$$B(z) = \frac{\mu_0}{4\pi} \frac{2\pi R^2 I}{(z^2 + R^2)^{3/2}}. \tag{4.1}$$

The radial component if the field is given by

$$B(r) = \frac{\mu_0 I z}{2\pi R r A} [E(k) \frac{1 + a^2 + b^2}{A - 4a} - K(k)], \tag{4.2}$$

where $a = \frac{r}{R}$, $b = \frac{z}{R}$, $A = (1 + a^2) + b^2$, $k = \sqrt{\frac{4R}{A}}$, $K(k)$ is the complete elliptic integral of the first kind, and $E(k)$ is the complete elliptic integral of the second kind. Using Eqs 4.1 and 4.2, we add the field component contributions from each coil (where the current direction is opposite for each coil). Due to dimensional constraints forced by the vacuum chamber, the coils were limited to 5 layers of thickness. We set the thickness and current as constants, 5 coils and 30 A respectively, and calculated that we needed 11 layers of loops for the height.

For testing, we mounted the coils apart from the vacuum chamber, but with the exact separation as would be used in the experiment. Using a hall probe, we measured the field at the center of the coil separation. Figure 4.3 shows the results of these measurements, which verified our calculations. As would be expected for an anti-Helmholtz configuration, the radial field gradient is half the value of the axial gradient.

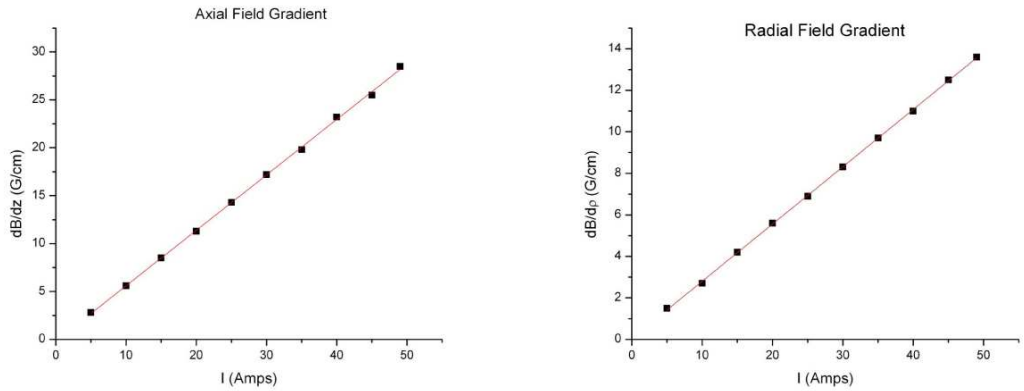

(a) (b)

Figure 4.4: (a) Measured axial field gradient from MOT coils. (b) Radial field gradient.

The thick kapton wire from which the coils are made is far to stiff to effectively wind by hand. Instead, we attached a plastic form to a lathe and manually rotated the lathe spindle to wind the coil around the form. Then we removed the coils from the form and coated each one with 5-minute epoxy.

When originally demonstrating the MOT, the coils were wired in series directly to the 50 A current supply. Later on, when performing characterizations of the MOT dynamics, we desired fast on-off switching capability for the magnetic-field. Due to very high inherent inductance of the coils, directly cutting power to the coils results in an 11 ms decay of the B-field. A simple on-off switch would not be sufficient to control the coils, since we wanted to measure dynamics much shorter than 11 ms.

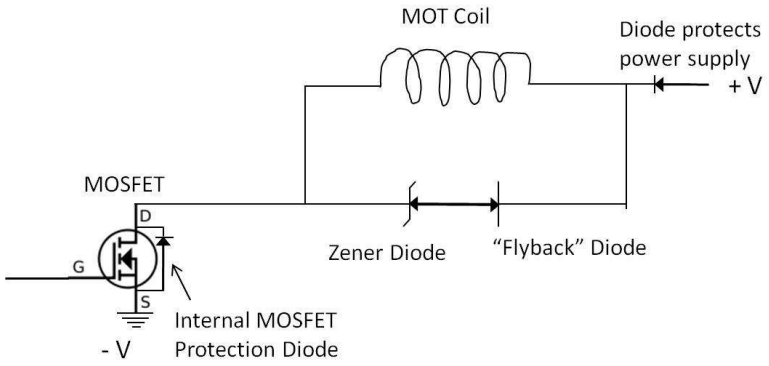

Figure 4.5: MOT coil switching circuit

To implement fast-switching of the B-field, we integrated the circuit shown in Fig. 4.5 into the coil circuit. A high power MOSFET (IXFN 180N15P) is placed in series with the the coils, and a zener fly-back diode (DSEP2x61-06A) is placed in parallel with the coils. When the coil current is shut off with the MOSFET, the zener diode overcomes the natural coil inductance, and rapidly discharges the

residual coil current. Using this circuit we measured a time constant of 110 µs. This time constant corresponds to the field decaying to 20% of its steady state value, after which the field decays much more slowly to zero.

In addition to the cooling and trapping coils, our system uses a set of shim coils to add offset corrections to the zero-point of the gradient B-field. This allows us to adjust the position of the MOT, ensuring formation at the zero-point. Please see Ref. [71] for extensive details of the shim coil design and construction.

4.4 MOT timing control

For measuring various MOT properties, including temperature, atom number, and density, we require a timing control system to synchronize the various shutters and electronics used in the measurements. The cooling beams, after exiting the mode cleaning optics, pass through a polarizing beamsplitter. The beamsplitter sends $\sim$5 mW to the saturated absorption setup, and the remainder of the power passes through an expansion telescope before going to the MOT. We placed a mechanical shutter at the beam waist of the telescope, where the waist size is 100 µs. The mechanical shutter is paired with a control unit which can be digitally triggered. We could not use an AOM in this situation due to the strong potential for damage from the high intensity UV light. With this shutter, we could practically extinguish the light to its 1/e intensity value at a rate of 1 ms.

In addition to the cooling beams, we need to control the camera exposure, the B-field, and the detuning of the MOT beams. We accomplish this using Arduino microcontroller boards, which are programmed to provide digital triggers to the

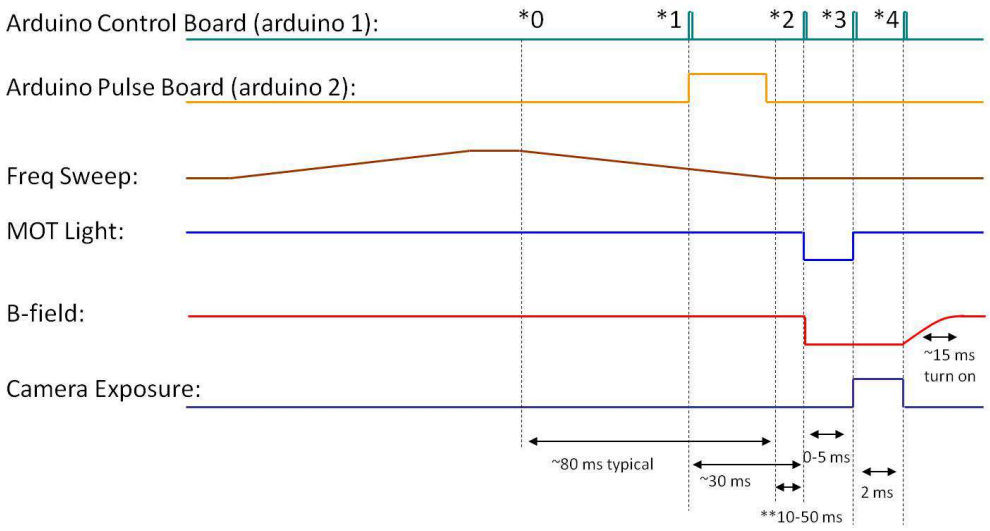

Figure 4.6: MOT timing diagram

camera, shutter, and B-field MOSFET. The detuning, which requires a sweep signal rather than just a TTL signal, is controlled using a National Instruments DAQ board. The top-level synchronization of the microcontrollers, DAQ board, data acquisition, and data processing is managed with a LabView program. Figure 4.6 shows a sample timing diagram used during an experiment to measure the MOT density.

CHAPTER 5

Characterization of the mercury MOT

Any neutral atom MOT posses an inherent set of dynamics which will dictate its usability for precision experiments. In the ideal case that our Hg MOT is used to load a lattice for precision clock measurements, it is critical to know the atom number, density, temperature, and loading rate of the MOT. In particular, the temperature will be directly relevant to how efficiently a lattice is loaded, and the atom number will have a direct effect on the clock accuracy. This is evident if we recall the clock stability parameter,

$$\sigma = \frac{\Delta\nu}{\nu_0}\sqrt{\frac{T_c}{N\tau}}. \tag{5.1}$$

5.1 Measuring the MOT atom number

We estimate a steady state atom number of 1-3 million atoms in our MOT. This is comparable to other Hg atom numbers reported in the literature, see Villwock et. al. [72]. The method we used to make this measurement is outlined below.

We use a Photometrics EMCCD to observe fluorescence from the MOT. The camera is sensitive in the deep UV, but the manufacturer does not provide response curves for the camera below 400 nm. After performing a measurement to calibrate the EMCCD response at 254 nm, we determined a conversion factor f_c that relates the total intensity count on the CCD to the incident UV energy in a 1 ms exposure

time.

To estimate the atom number in the MOT, we assume a spontaneous emission rate of $\gamma_{\mathrm{sp}} = 1.27$ MHz and a stimulated emission rate γ_{st}. For low intensity cooling beams, the stimulated emission rate is a small fraction of the spontaneous emission rate. To find the number of atoms radiating into 4π steradians, we subtract the number of stimulated emission events from the number of spontaneous emission events. The total energy of the fluorescence from the spontaneous emission events of N atoms is then given by

$$E = N(\gamma_{sp} - \gamma_{st})h\nu t \tag{5.2}$$

To translate Eq. 5.2 to the number of intensity counts, n_c, on the EMCCD, we must incorporate the collection area, $\frac{3r_w^2}{4r_{ch}^2}$, the transmission factor of the bandpass filter, f_t, and the aforementioned conversion factor, f_c.

The number of atoms N in the MOT is given by

$$N = \frac{4n_c r_{ch}^2}{3(\gamma_{sp} - \gamma_{st})f_t f_c h\nu t}. \tag{5.3}$$

With a detuning of 2.5 MHz, a cooling beam intensity of $3\mathrm{I}_{\mathrm{sat}}$, and a background pressure 2×10^{-9} torr, we calculate an atom number of 2.6×10^6. The atom number varies strongly with intensity and detuning. As background pressures increase, the atom number will increase, until a certain point at which the number of background collisions increase the loss rate of the MOT. Figure 5.1 shows the MOT intensity images used to calculate the atom numbers, as well as other parameters.

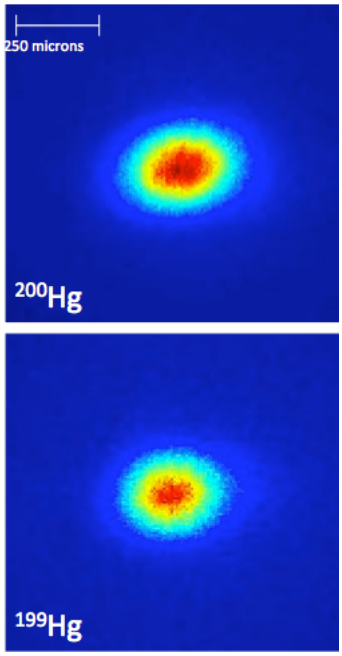

Figure 5.1: MOT intensity profile for ^{199}Hg and ^{200}Hg

5.2 Measuring the MOT density

To determine the MOT density, we must define a measurement volume. Under the assumption that our Hg MOT will eventually be used to load a lattice trap, we chose a 37 µm cubic volume at the center of the MOT. The center of the MOT should have the highest concentration of low energy atoms, which makes it the most ideal region from which to load a lattice.

The density measurement is accomplished using the timing sequencing described in Chap. 4. First the detuning from the cooling transition is swept from -1 MHz to -5 MHz, then back to -1 MHz over an 80 ms period. This results in a momentary density 2-3 times higher than the steady-state density. The CCD is programmed to image the MOT immediately after the sweep, before the density returns to a steady

state value. The CCD image of the MOT is processed in LabView and MATLAB using a modified 2D Gaussian fit routine which is publicly available from National instruments [73].

When performing the fitting, we must consider the fact that the 2D fit does not account for the depth of the trapped atom cloud. We add in a correction factor, which typically reduces the density by a factor of 15 over the uncorrected 2D calculation. Using this method we found a density for our MOT in the range of 5×10^{10} to 2×10^{11} atoms/cm^3

5.3 Measuring the MOT loading time

Understanding the loading time of a MOT is important for spectroscopic measurements. Several factors come into play when determining how quickly a MOT should load from from the background vapor [74]. The rate equation describing the number of atoms in a MOT, assuming low densities, is given by

$$\frac{dN}{dt} = -\Gamma_L N + R_L \tag{5.4}$$

where Γ_L is the collisional loss rate and R_L is the loading rate. Solving this equation, we find

$$N(t) = \frac{R_L}{\Gamma_L}(1 - e^{-\Gamma_L t}). \tag{5.5}$$

To take the loading time data, we shut off the cooling beams (using a shutter), acquire a background image, then open the shutter and acquire the loading time data for several seconds. The shutter is then closed again. The timing is controlled by the Arduino microcontroller boards.

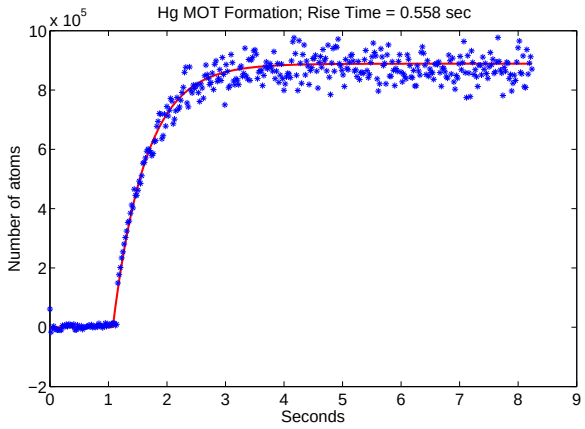

Figure 5.2: Loading time data at a background pressure of 2×10^{-9} torr.

The full loading time data, relative to background vapor pressure, can be found in Fig. 4.3 in Chap. 4, Sec. 4.2. Figure 5.2 shows a single set acquisition of the loading time at a background pressure of 2×10^{-9} torr. We did not take data for loading times less than 75 ms, as this approaches the time resolution of our CCD.

5.4 Measuring the MOT temperature

The steady-state temperature of the MOT atoms will determine how much intensity is required to load a lattice trap. The Doppler-limited temperature for a mercury MOT, defined at the limit of zero intensity and one linewidth of detuning, is 31 µK. This is a sufficiently low temperature for efficiently loading a lattice. Unlike ytterbium and strontium, mercury does not require two-stages of cooling to reach the doppler-limit temperature.

Doppler theory gives an expression for the doppler-limit:

$$T_D = \frac{\hbar\Gamma^2}{8k_B\Delta}(1 + \frac{I}{I_s} + \frac{4\Delta^2}{\Gamma^2}), \tag{5.6}$$

where $\Gamma = 2\pi \times 1.3$ MHz, Δ is the detuning from resonance, I is total MOT beam intensity, and I_S is the saturation intensity for the neutral Hg ground state transition. The neutral Hg cooling line intensity is 10.2 mW/cm^2. Differentiating Eq. 5.6 to find the detuning at the minimum temperature yields (holding I constant),

$$\Delta = \frac{\Gamma}{2}\sqrt{1 + \frac{I}{I_s}}. \tag{5.7}$$

Figure 5.3 shows the theoretical curves for MOT temperature vs detuning and intensity. Substituting Eq. 5.7 into Equ. 5.6, and taking the limit of zero intensity, we find the doppler-limited temperature:

$$T_D = \frac{\hbar\Gamma}{2} \tag{5.8}$$

For our MOT system, we describe three techniques for measuring the temperature. The first two are variations of a time-of-flight ballistic expansion method, and then in the final method we derive temperatures from the doppler-broadened linewidth of the clock transition.

5.5 Time-of-flight temperature measurement method

Our initial method for measuring the temperature involved ballistic expansion of the trapped atoms. Under steady state conditions, the MOT has a 3D guassian profile, with a radius governed by the strength of the magnetic field gradient. When the cooling beams are shutoff, the trapped atom cloud will expand at a rate related to the velocity distribution of atoms in the cloud. The radius of the MOT cloud at a particular time t is given by

$$r(t)^2 = r_0^2 + \frac{k_B T}{m} t^2, \tag{5.9}$$

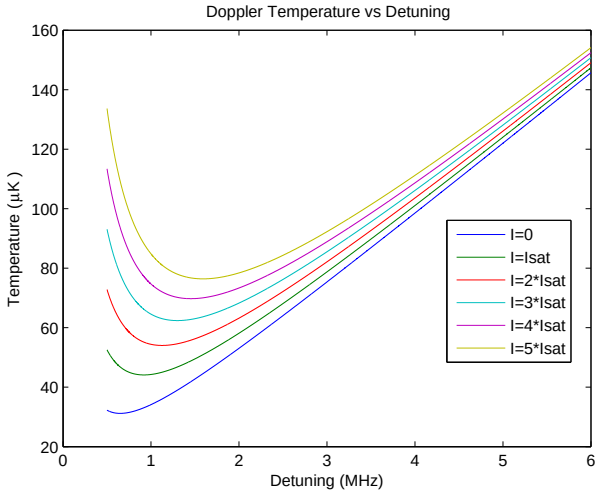

Figure 5.3: Doppler temperature curve. At a given intensity, the minimum temperature occurs at a detuning that coincides with the power-broadened linewidth.

where r_0 is the initial MOT radius, m is the mass of a single Hg atom, and T is the temperature. This equation encapsulates the time-of-flight method. We can use our timing system and EMCCD to image the MOT fluorescence and measure the MOT radius at different expansion times. We then apply a linear regression to determine the coefficients in Equ. 5.9.

The timing schematic for the fluorescence measurements is shown in Fig. 5.4. We use the detuning sweep technique to achieve the highest possible MOT density and atom number. While the MOT is compressed, the cooling beams are shut-off, then 100 μs later, the magnetic field is turned off. The MOT cloud is allowed to expand for a duration varying from 1-3 ms, at which point the cooling beams are turned on in order to image the MOT cloud. The image data is sent to a LabView program which calculates the radius.

During these measurements, we discovered that the temperature of the MOT

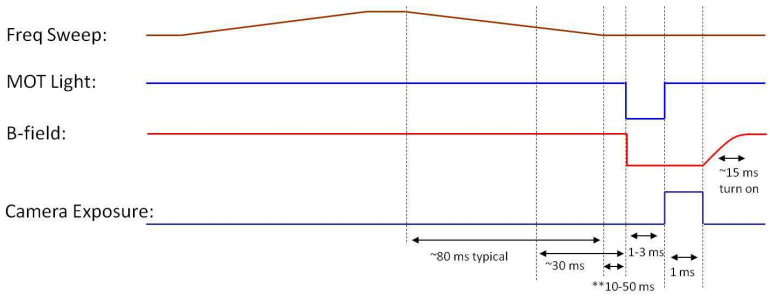

Figure 5.4: Time setup used for the fluorescence measurements.

was heavily dependent on the exposure time of the EMCCD (see Fig. 5.5). After several rounds of testing, we concluded that using the cooling beams as an imaging light was causing the MOT to re-form, even during the brief 2 ms exposure time. We attempted to rectify this problem by shutting off the magnetic field for each measurement. In this case, the SNR of the measurements was too low to make any valid conclusions. Other temperature calculation experiments in the literature did not see the same dependance on camera exposure time. To cross-check the fluorescence-based measurements, we implemented an absorption scheme.

To setup the absorption measurement, we pick off a small portion of the UV cooling light between the two AOMs used to set the detuning. At this point, the picked off light is shifted $\sim$ 200 MHz below resonance. We then send the beam through a second AOM, which shifts the beam back into resonance and serves as a fast switch. The switched on beam interacts with the MOT and is imaged by the EMCCD. We attenuate the beam to protect the EMCCD from damage.

The timing schematic for the absorption measurements is shown in Fig. 5.6. In this case, we must take two images: one of the MOT expansion and one "dark" background image. The fast switching time of the AOM allows us to take images for

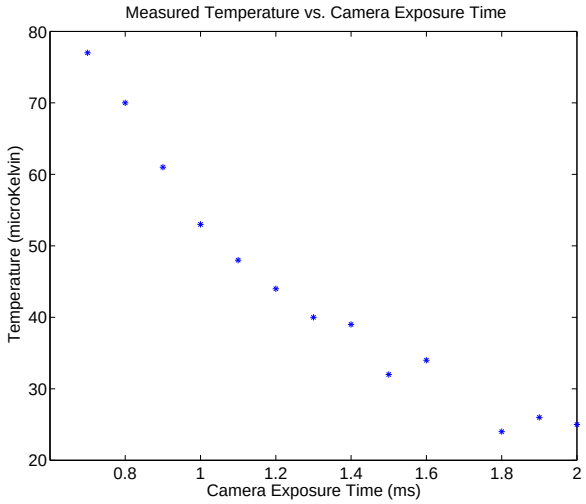

Figure 5.5: The MOT temperature fluorescence measurements show a strong, unexpected, dependence on the camera exposure time.

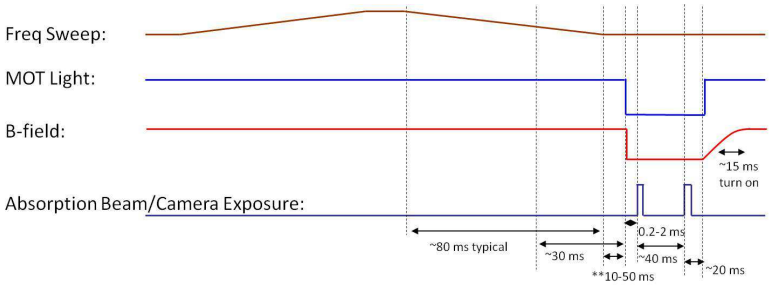

Figure 5.6: Time setup used for the absorption temperature measurements.

expansion times below 1 ms, avoiding an unfortunate limitation of the fluorescence measurements.

The absorption expansion images are analyzed by our LabView fitting routine. From this data, we derived an approximate MOT temperature of 80-130 µK, which agrees well with our lower-bound estimate from the fluorescence measurements. The large error arises from SNR issues with the absorption measurements.

CHAPTER 6

Spectroscopy of the ^{199}Hg clock transition

6.1 Method for observing the Hg clock transition

The cooling laser and the vacuum chamber prepare the mercury for probing with the spectroscopy laser. Though the end goal of this system may be a complete lattice clock, we must first demonstrate spectroscopy of the doppler-cooled atoms, directly inside the MOT. To make a measurement of the doppler-broadened 6^1S_0 - 6^3P_0 transition, we use a direct excitation scheme first implemented by [75]. Using a probe laser tuned to the clock transition resonance, the probe beam is aligned to intersect the cold atom cloud in a Doppler-free configuration. As the probe laser is tuned to the clock transition frequency, a small percentage of the MOT population is excited to the long-lived $^3P_0$ state. The atoms begin to fall out of the trapping region, Doppler-shifting out of resonance with the cooling beams. In a fraction of a second, the atoms have left the capture region, and have been removed from the cooling transition cycle. These atoms will eventually weakly fluorescence at the 265.6 nm clock wavelength. However, since the transition probability is small, the fluorescence will be extremely weak, and would be very difficult to distinguish from the 254 nm cooling light. To observe the clock transition, we instead use indirect detection. By monitoring the steady-state fluorescence of the MOT at 254 nm, we can observe a drop in fluorescence as the atoms are cycled out of the cooling

transition by the clock laser. This amounts to a much more sensitive detection technique than direct observation of the clock transition upper state fluorescence. If the doppler-free alignment is optimized, and the clock laser linewidth is sufficiently narrow, this technique should also reveal the recoil-doublet peaks [31].

The rate at which atoms are excited to the clock transition will depend on the frequency scan rate, probe beam power, and spatial overlap with the MOT. As atoms fall out of the capture region, the cooling beams are continuously loading the MOT from the background vapor pressure. We must ensure that the probe beam depletes the MOT faster than the loading rate (dictated by the background pressure, see Chap. 5, Sec. 5.3). Otherwise, the fluorescence dip will be difficult, if not impossible, to detect.

If the transition is scanned while the cooling beams are on, the measured transition frequency will be offset by the AC stark shift effect. To account for the stark shift, we can perform a field-free measurement, where the MOT beams are cycled off as the probe laser scans the transition. This type of measurement has been performed on several optical clock systems [31, 75, 76]. In this section, we also describe our characterization of the stark shift. The magnitudes of other induced shifts, such as those from magnetic fields and blackbody fields, are well below our current level of measurement precision.

6.2 Clock spectroscopy laser

Taking a similar tactic as the cooling laser system, we begin with an IR source and use external frequency doubling to generate the 265.6 nm clock light. Although

our initial spectroscopy data only resulted in observation of the Doppler-broadened 6^1S_0 - 6^3P_0 transition, our clock system includes a frequency stabilization setup for achieving hertz-level linewidths. This would be necessary for full-resolution lattice spectroscopy of the sub-hertz clock transition [30].

The IR probe laser source and doubling cavities are shown in Fig. 6.1. The IR source is a commercial NP Photonics Rock ytterbium fiber laser, with a free-running linewidth of approximately 7 kHz. The probe laser has a piezo actuator with a scan range of ± 250 MHz and a rated bandwidth of 30 kHz. In practice, we found the effective piezo bandwidth to be 3 kHz. We are not certain of the reason for the large discrepancy in measured versus rated bandwidth. The probe laser generates 70 mW of power at 1062 nm, which is amplified using a 2 W Nufern fiber amplifier. The AOM and the second fiber amplifier shown in Fig. 6.17 were not used in the original clock transition measurement experiment. These were included later on during the photon recoil search and the two-photon experiment.

To generate the intermediate green light at 531 nm, we collimate and then focus the amplified IR into a 4 cm long periodically-poled lithium niobate (PPLN) crystal. The crystal is quasi-phase matched at an optimal temperature of 81 °C. During operation of the system, we have found that the phase-matching temperature varies 0.1-0.4 °C depending on the humidity. With 1.7 W of incident power at 1062 nm, we are able to generate 130-140 mW of green light. The green light is then collimated and a dichroic mirror is used to separate out the residual fundamental light. The separated fundamental is strongly attenuated and coupled into a fiber for transfer to the reference laser system. The reference laser system will be described in Sec.

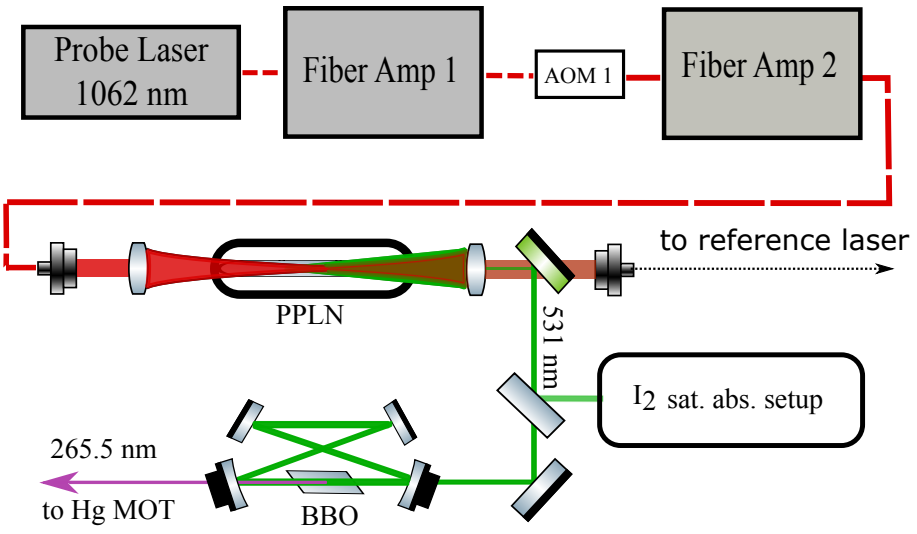

Figure 6.1: Probe laser system for scanning the clock transition. Fiber Amp 2 was inserted after the initial spectroscopy measurements to facilitate the two-photon measurement (Sec. 6.17)

6.8.

Generating sufficient UV power at 265.6 nm requires the use of a ring-resonator doubling cavity. We use a 7 mm AR-coated BBO crystal for the nonlinear element. The crystal is mounted to allow for adjustment in the axial and azimuthal planes. A peltier device keeps the crystal temperature slightly above room temperature (∼27 °C) to protect against condensation. The cavity is approximately 86 cm in length and the two curved mirrors have a ROC of 10 cm. The second curved mirror is a dichroic, designed to transmit over 95% of the second harmonic UV light. One of the flat cavity mirrors is mounted to a piezo for locking of the cavity resonance using a polarization locking scheme [53]. Although this BBO crystal is not Brewster cut, we can place a λ/2-WP before the cavity to generate a differential loss between 's' and 'p' states in the cavity. The difference is strong enough to produce a large error

signal for the polarization lock. From 140 mW of 531 nm light, we can generate up to 15 mW at 265.6 nm. Based on previous measurements of the Doppler-broadened transition [31], we chose not to spend further time extracting more UV power from the system.

6.3 Absolute iodine frequency reference

The frequency of the ^{199}Hg transition has been given, in absolute and very precise terms, by McFerran et. al. [33]. To find this frequency, we require an absolute starting point. Many optical clock experiments use a frequency comb referenced to another stable clock to establish an absolute standard for a precision frequency measurement. We do not have access to a high-precision wavemeter, let alone a separate stable atomic clock. Our Burleigh WA-110 has an effective precision of ± 2 GHz in the UV, which is inadequate for finding the 1 MHz linewidth clock transition. To remedy this situation, we searched for an atomic reference that could provide MHz level precision. Aware of the fact that molecular iodine (I_2) has many roto-vibrational transitions near 532 nm, we located a group of (I_2) lines closer to 531 nm (half the frequency of the Hg clock transition). This grouping is located 1.1 GHz below the ^{199}Hg transition in IR frequency space. These lines are were found in a comprehensive atlas of molecular iodine transitions produced by Kato et. al. [77]. Figure 6.2 shows the grouping.

To make use of these lines, we built a saturated absorption experiment using the green light generated from the PPLN. To pick off the light, we simply use the back-reflection from the UV doubling ring cavity. This requires blocking the cavity

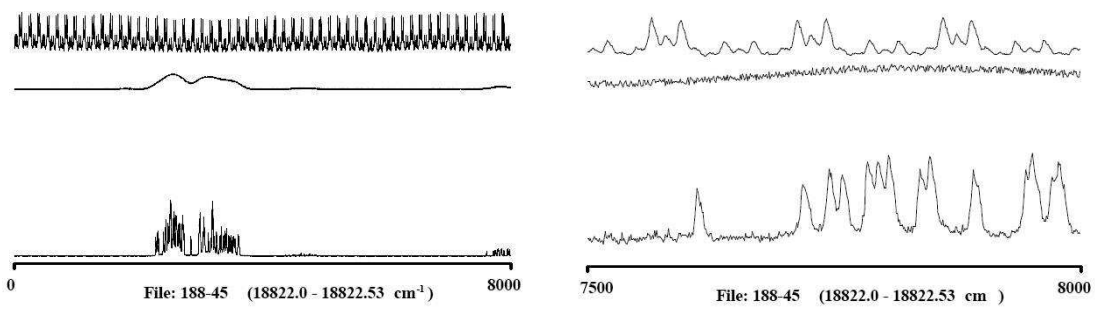

(a) (b)

Figure 6.2: (a) Iodine atlas entry (figure borrowed form Kato et. al. [77]) used for clock spectroscopy reference line (far right grouping). (b) Zoom in scan of grouping from atlas.

resonance in order to avoid random intensity fluctuations as the green light passes through the cavity resonance. We also note that this prevents us from locking the UV cavity while observing the iodine lines. Using the back reflected light, we have at our disposal approximately 80 mW at 531 nm for the saturated absorption setup. Since the I_2 lines are weak, we need a generous amount of power to resolve the lines. However 80 mW is excessive, so we attenuate the light to 20 mW. The iodine grouping, resolved with our apparatus, is shown in Fig. 6.3.

Generating the calibrated axis shown in Fig. 6.3 is accomplished using a phase-locked loop and optical heterodyne detection. We first tune a separate Toptica diode laser to 1062 nm and implement an FM lock to stabilize the Toptica laser to an ultra-high finesse Fabry-Perot cavity manufactured from ultra-low expansion glass (see Sec 6.6). We then form a heterodyne beatnote between the Toptica laser and the fundamental of the probe laser, and use this as the VCO input to a phase-locked loop circuit. We can then tune the probe laser relative to the stabilized

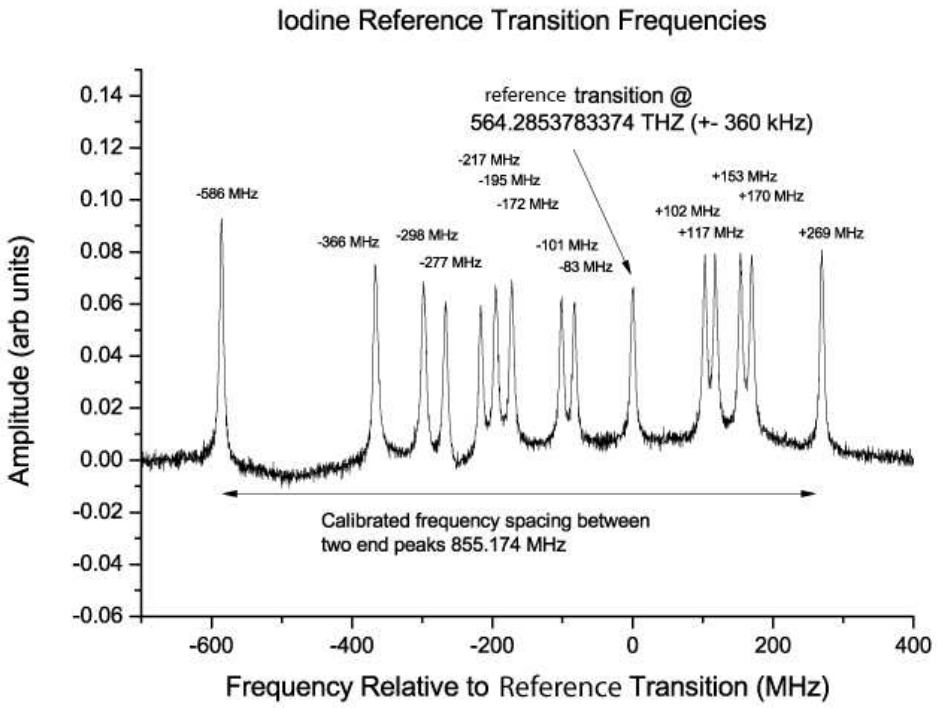

Figure 6.3: Scan of the iodine grouping, showing the specific line used to reference the ^{199}Hg clock transition.

Toptica laser to measure the linewidth and frequency spacing of the iodine lines.

Out of this grouping, we have identified one line to serve as the reference (see Figure 6.3). Visual inspection of the atlas [77] yields an approximate frequency of 564285.3858 $\pm$ 0.0143 GHz for this line. The uncertainty value arises from the $\pm$4.3 MHz uncertainty given by the atlas, and the $\pm$10 MHz linewidth of the identified peak. After finding the Hg clock transition, we measured a more precise value for the iodine. This measurement is described in more detail in Sec. 6.14.

6.4 Probe laser apparatus

The other crucial component of the spectroscopy system is the stabilization setup. The primary role of this setup is to narrow the probe laser linewidth and minimize the long-term drift of the probe laser. The iodine reference setup discussed in Sec. 6.3 is directly coupled to the probe laser. It is not technically feasible to span the 1.1 GHz frequency gap between the iodine reference and the Hg transition using AOMs, resulting in a situation where we cannot simultaneously lock to the iodine and shift the probe laser to the clock transition. Likewise, without the AOMs, we could not simultaneously lock to a stabilization cavity and tune towards the clock transition. While it would be possible to use a large bandwidth EOM, budgetary constraints prohibited such an option at the time we were assembling the system.

To solve this dilemma, we decided to use a secondary laser, what we call the reference laser, as a stability transfer mechanism. The reference laser would directly lock to a stabilization cavity, and then the probe laser would lock to the reference laser using a phase-locked loop. The advantage in this setup arises from the fact that the probe laser inherits the narrow linewidth of the reference laser, and can be phase-locked at an offset from the reference laser, allowing the system to scan the clock transition and remain locked to a stabilization cavity.

Figure 6.4 shows the entire spectroscopy system, including the probe laser, reference laser, iodine reference, and stabilization cavity. In the following sections, we describe in detail the stabilization and reference components. Both the first and second generation of this system are discussed.

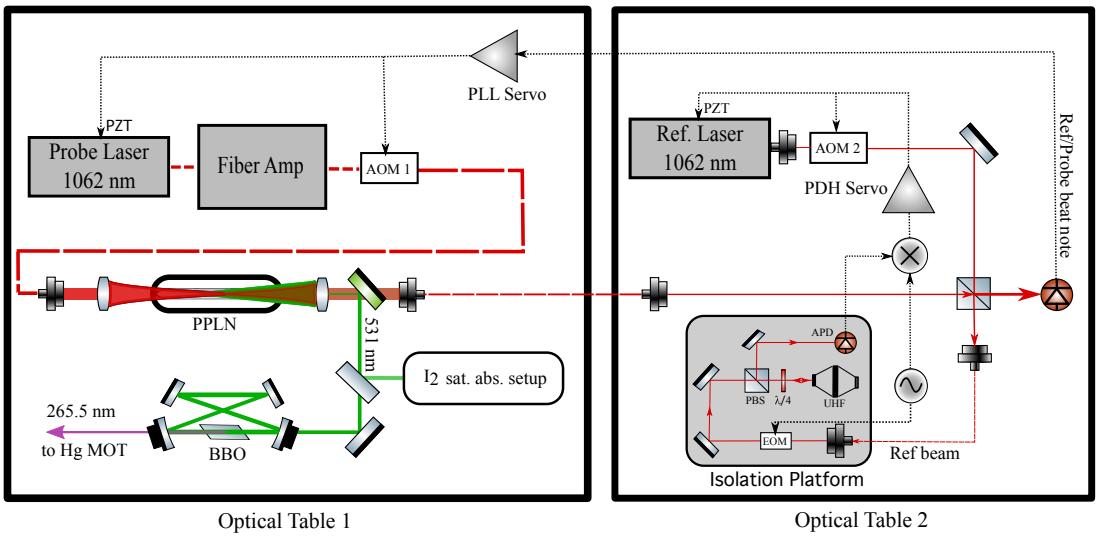

Figure 6.4: Clock spectroscopy apparatus, showing probe laser and reference laser. The reference laser locks to the high-finesse cavity using a PDH lock and the probe laser locks to the reference laser using a phase lock.

6.5 Low-finesse stabilization cavity

The first generation reference laser was a Toptica DL-Pro ECLD. The laser includes a high-bandwidth current control and PZT, and has a free-running linewidth of approximately 100 kHz. Before aligning this laser to the ultra-high finesse UHF (Ultra-high Finesse) cavity, we performed stability testing with a much lower finesse zero-dur cavity. The cavity was isolated from the environment using foam panels inside a wood box (See Figs. 6.5a, 6.5b). To characterize the drift rate of the cavity, we locked the Toptica to this zero-dur cavity and locked the probe laser to the iodine reference. We then formed a heterodyne beat note between the two stabilized lasers. Figure 6.5c shows data from monitoring the beatnote frequency. The large frequency drifts result from the strong sensitivity of the cavity to changes

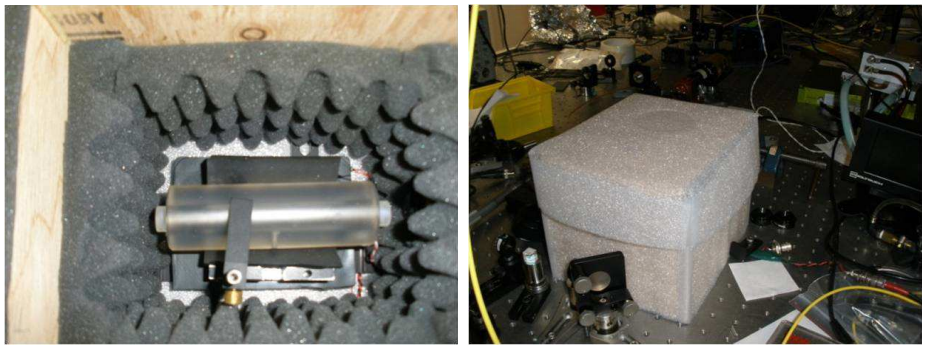

(a) (b)

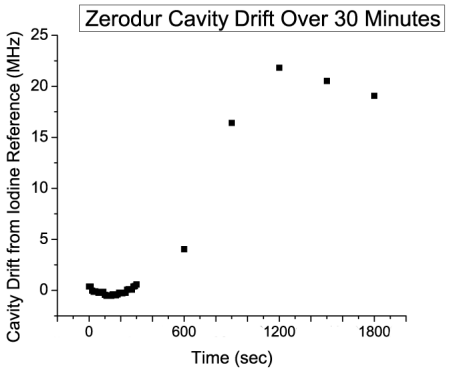

(c)

Figure 6.5: (a)(b) Low-finesse zero-dur reference cavity with environmental isolation (c) Cavity drift over 30 minutes. The sharp increase after 5 minutes is the result of a sudden change in the thermal environment near the cavity.

in the thermal environment. From this data, we concluded that the cavity thermal characteristics and environmental isolation provided insufficient stability levels for scanning the 1 MHz clock transition. The cavity was simply too sensitive and too responsive to thermal changes.

6.6 Ultra-high finesse cavity apparatus

In light of the poor stability results from the low-finesse cavity, we quickly moved forward implementing an isolation system for the ultra-high finesse (UHF) cavity we obtained from Advanced Thin Films. The cavity is manufactured from ultra-low expansion glass (ULE). To optimize the isolation, we must protect the cavity from mechanical noise, thermal noise, and pressure fluctuations. To this end, we use a commercial Minus K isolation platform, a custom built vacuum chamber, and copper shielding. We do not currently implement active thermal stabilization, which will be required to reach Hz-level linewidths. In the ideal case, the zero-point expansion temperature of the cavity will be measured and held constant with a temperature control system, resulting in minimal drift of the cavity.

Figure 6.6 shows the vacuum chamber we designed to house the UHF cavity. The chamber is an aluminum cylinder, with two 1" window ports on the top and the bottom. A pump connection port is welded to the side of the cylinder. All the flange seals use Viton o-rings, except for the pump tee, which uses Conflat flanges. One end of the tee connects to a 20 L/s Duniway ion pump, and the other end connects to a mating flange for attaching a turbo pump. The windows are AR-coated near 1062 nm and manufactured with a 0.5" thick substrate to account for stress experienced under low vacuum. The windows are attached to the chamber by pressing the outer window edge directly against an o-ring using a donut shaped piece of aluminum. The cavity is supported by a teflon mount, which rests on top of an o-ring placed on the bottom surface of the aluminum cylinder. We also placed

a copper shield around the cavity with a small opening at the top to pass light transmitted through the cavity. The cavity transmission is monitored using a basic CCD camera mounted to the top of the aluminum cylinder.

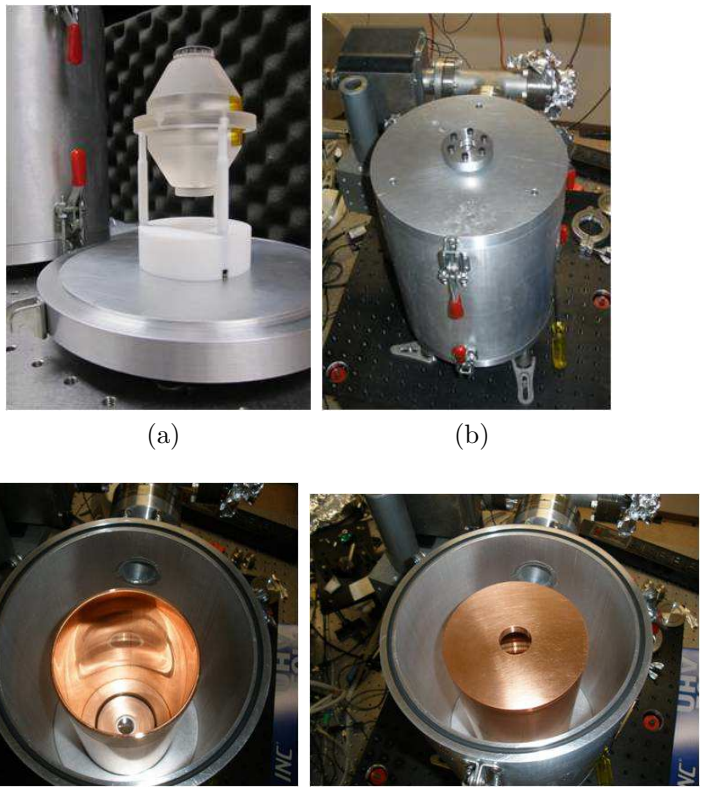

Figure 6.6: (a) 10 cm length ULE cavity. (b) Aluminum vacuum chamber. All flanges are sealed with viton o-rings, except for the pump tee. (c),(d) Copper heat shield provides passive thermal isolation to the cavity.

Previous information from the literature [78] indicates we only needed a vacuum level of 10^{-7} torr. To achieve this, we performed a basic bakeout of the chamber.

6.7 Ultra-high finesse cavity characterization

The UHF cavity has an expected finesse between 400,000 - 700,000. For narrow linewidth cavities, it is very difficult to fully resolve the cavity linewidth in order to directly measure the finesse. This is particularly true if the laser linewidth is greater than the cavity linewidth. Instead, we can take advantage of the long photon lifetime inherent to high finesse cavities. The long photon lifetime will result in a resolvable chirped ring-down signal, with a decay constant proportional to the finesse. The ring down signal is modeled by

$$f(t) = Ae^{-t/\tau}sin(at + bt^2 + c), \tag{6.1}$$

where the chirped sinusoidal term results from the interference between the incident and cavity leakage light. We care primarily about the exponential term, τ, which is related to the finesse by

$$F = 2\pi\tau \times FSR, \tag{6.2}$$

where FSR is the free spectral range of the cavity. Using this simple model, we measured the cavity finesse with the fiber probe laser. Figure 6.7 shows the ring-down signal along with a fit to the model in Equ. 6.1. The finesse in this measurement is 586,941. A group of six measurements yielded an average finesse of 630,000.

6.8 Spectrosopy apparatus details

Referring to Fig. 6.1, we can see that the UHF cavity is mounted on the stabilization platform. A few milliwatts of light from the reference laser are coupled onto the

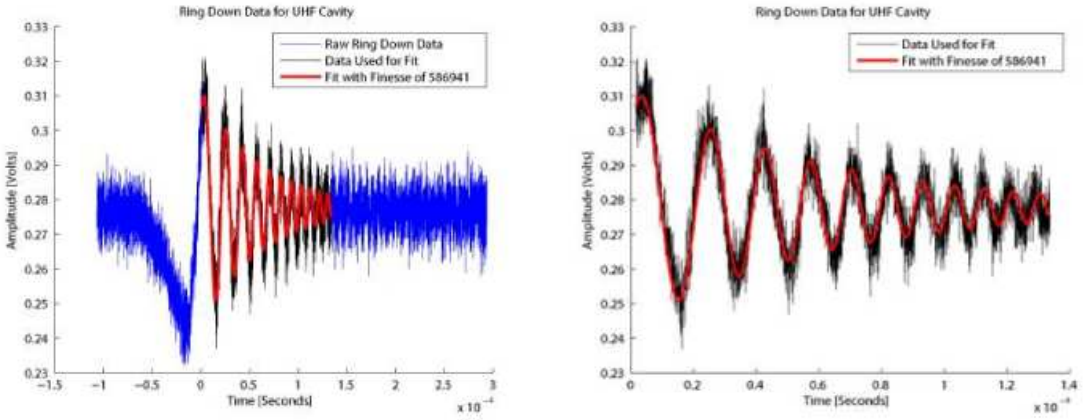

(a) (b)

Figure 6.7: Chirped ring-down signal used to derive the cavity finesse. Average cavity finesse is 630,000.

platform via a short length of non-PM fiber. Once on the platform, the light passes through an isolator, $\lambda/2$ waveplate, polarizing beamsplitter, and EOM. The EOM, a NewFocus 4005 model, is resonantly driven at 10.7 MHz. After the EOM, the light is steered into the cavity using a standard optical configuration for generating a PDH error signal. A nano-particle grating is placed before the PDH polarizing beamsplitter in order to attenuate the power to $\sim$ 10 µW. A low incident power level is necessary to protect the UHF cavity end-mirrors from damage. With a finesse of 600,000, the intra-cavity intensity will increase rapidly, and with even a few milliwatts of incident power, would quickly reach damaging levels. Finally, we use a Thorlabs APD110A2 avalanche photodiode to detect the reflected cavity light.

For the first generation reference system, there was no AOM used in the spectroscopy setup, as the ECLD laser has a built-in fast current control. The second generation system, which uses an NP Photonics Rock ytterbium fiber laser for the

reference laser, required an AOM, since the Rock laser has only slow piezo feedback capabilities. The 200 MHz AOM is a free-space model, necessitating a short section of free-space optics between the Rock laser and the fiber link to the isolation platform. To summarize, the first generation reference laser used a combination of piezo and current control, both built into the ECLD, for feedback correction; the second generation system uses the internal fiber piezo in combination with an external AOM.

The final part of the spectroscopy setup involves the probe laser (see Fig. 6.1). The first generation system did not use the AOM or secondary amplifier shown in Fig. 6.1. The feedback correction was limited to the fiber piezo. The second generation system added in a fiber-coupled 150 MHz AOM (Gooch & Housego Fiber-Q) for much faster frequency bandwidth. The secondary amplifier is a special upgrade for performing the two-photon experiment described in Sec. 6.17. The probe laser system and the reference laser system are built on separate optical tables, since the isolation platform cannot be placed on an air-suspension lab table. To link the two laser systems, we route a fraction of the excess fundamental probe light (1062 nm) to the reference laser table through a non-PM fiber. The reference beam and probe beam are then mixed in a beam splitter to form a heterodyne signal, which is fed to a phase-locked loop circuit and a PID servo. This servo sends frequency corrections to the probe laser.

6.9 Linewidth control of the probe laser

Although our spectroscopy results (presented in Sec. 6.11) only occurred in the Doppler-broadened MOT regime, a full-scale lattice clock would require a Hz-level linewidth probe laser. With the ultimate goal of a lattice clock in mind, we pursued building and characterizing the apparatus necessary for Hz-level linewidth stabilization. In the first generation system, we never achieved a linewidth below the 7 kHz free-running linewidth of the probe laser, due primarily to the poor feedback bandwidth of the fiber piezo. Based on data gathered on the beat note between the ECLD reference and the probe laser, the bandwidth of the probe piezo is 3 kHz. This was insufficient to reduce the linewidth by any appreciable amount. In fact, when the ECLD was locked to the UHF cavity and the probe was phase-locked to the ECLD, the beat note FWHM was $\sim$10 kHz, indicating the PLL lock was weak. This implies that the stability of the ECLD was not being transferred to the probe laser. Nevertheless, despite these poor results, we were able to use this setup to scan the doppler-broadened clock transition. The piezo was fully capable of accounting for any slow drifts of the spectroscopy system, which proved sufficient for the doppler-broadened spectroscopy.

The second generation system, which substitutes the ECLD for a fiber laser/AOM combination and incorporates a fast AOM into the probe laser system, yields much better results for the linewidth stabilization. We use a fast commercial PID servo (VESCENT) to lock the reference fiber laser to the UHF cavity, and the phase lock between the probe and reference lasers utilizes an in-house PI servo.

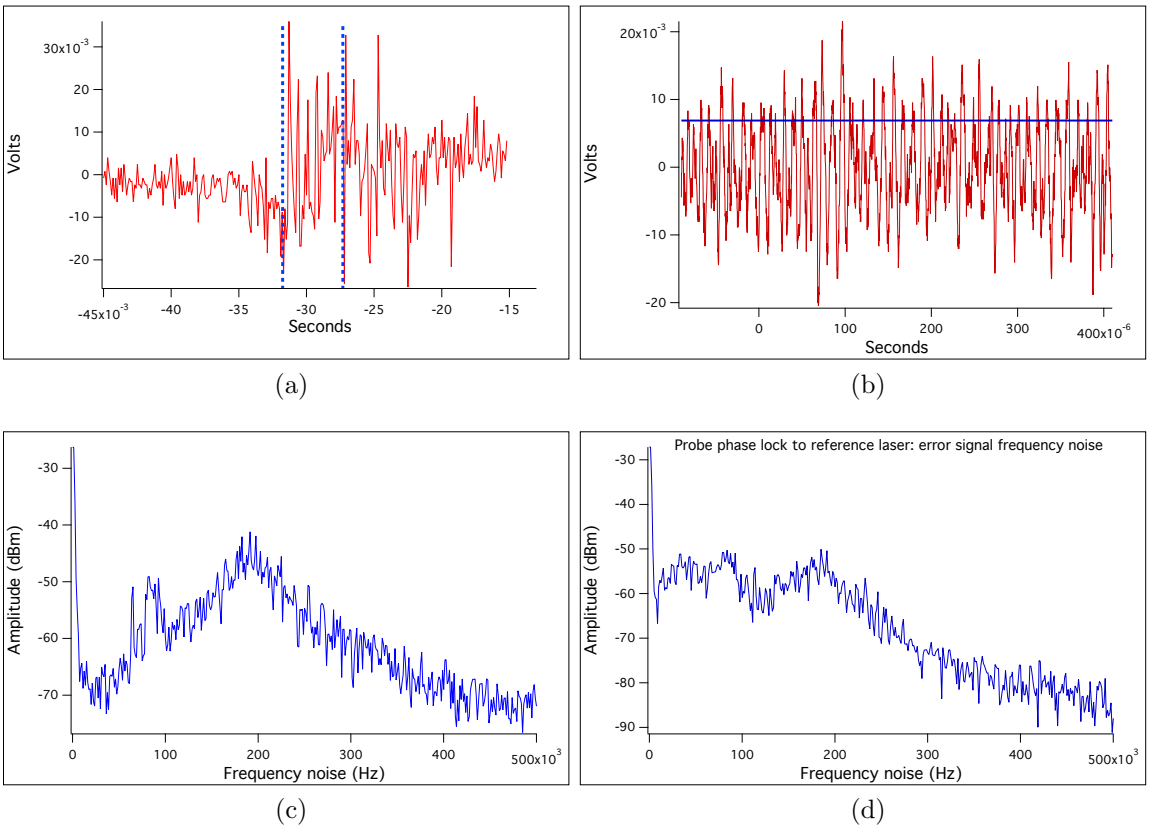

Figure 6.8: (a) Slow scan of UHF cavity error signal with the fiber reference laser. Dashed lines mark the FWHM of the derivative signal. (b) Locked error signal. Blue line marks the RMS voltage, which is used to estimate the linewidth. (c) Power spectrum of the reference laser error signal while locked to the UHF cavity. (d) Power spectrum of the phase-lock error signal, showing gain bandwidth of 200 kHz.

We evaluated the probe lock to the UHF cavity using basic metrics related to the RMS linewidth of the locked error signal. Figure 6.8 shows data evaluating the lock parameters from the power spectral densities of the error signals as well as direct measurement of the error signal voltage. Using the RMS measurement, we estimate a reference laser linewidth of 525 Hz. The power spectrum data indicates both locks have a bandwidth of ∼200 kHz.

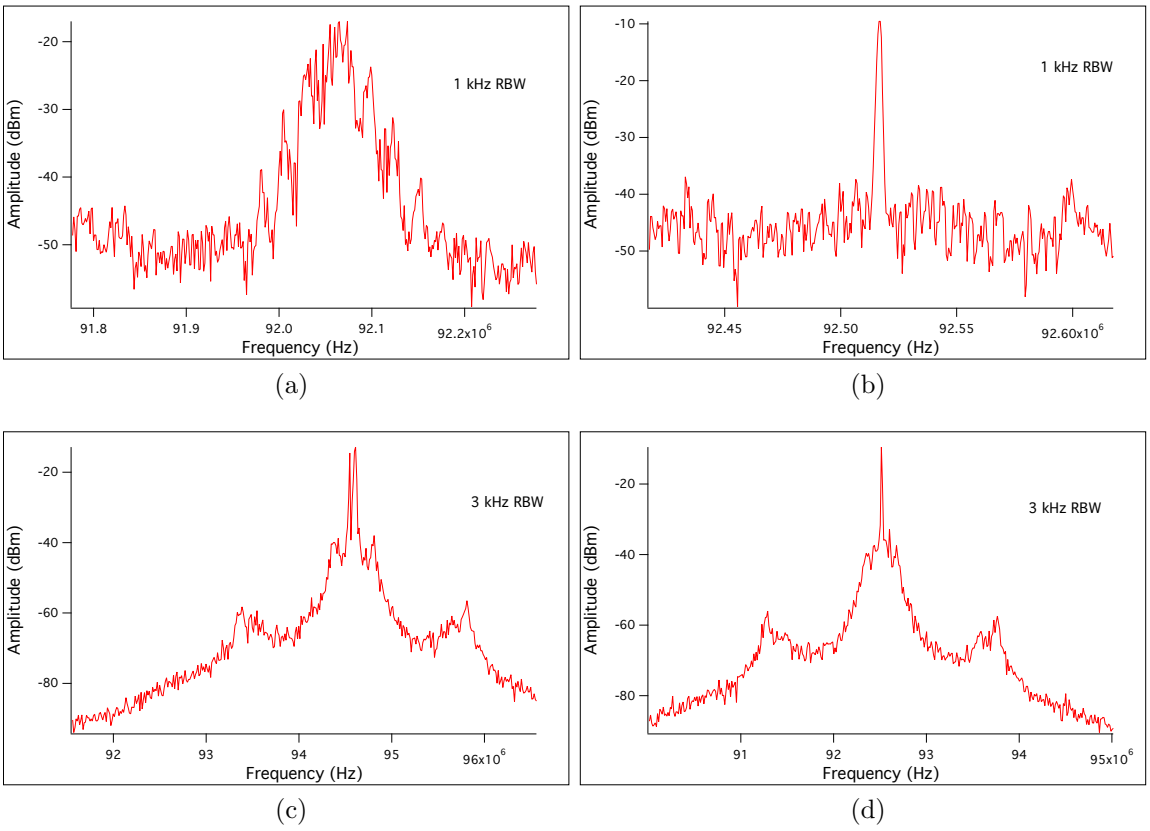

Figure 6.9: Heterodyne beatnote between the reference and probe laser. We were able to resolve the beatnote down to the 1 Hz resolution bandwidth of the spectrum analyzer, suggesting a tight phase lock between the lasers. Sidebands near 1.5 MHz result from RIN noise and relaxation oscillations in the fiber lasers. (a) Beatnote with system unlocked; resolution bandwidth (RBW) is 1 kHz (b) Beatnote with system locked; RBW = 1 kHz (c) Beatnote, system unlocked; RBW = 3 kHz (d) Beatnote, system locked; RBW = 3 kHz.

With this system, we demonstrate the ability of the PLL to transfer the full stability of the reference laser to the probe laser. Figure 6.9 shows data from the heterodyne beatnote between the reference and probe laser. Measurements of this beatnote between the lasers while both locks are active provides information about the relative linewidth between the two lasers. Any non-zero width of the beat note

suggests phase-noise is being added to the reference linewidth upon transfer to the probe system. We were able to resolve the beatnote down to the minimum 1 Hz resolution bandwidth of the spectrum analyzer, suggesting a very tight phase lock and minimal addition of phase noise during transfer. Figures 6.10 demonstrates an alternate way to measure the reference laser servo gain bandwidth. The sidebands which appear near 200 kHz are a result of gain oscillation in the reference servo when the proportional gain is increased towards the closed-loop bandwidth of the system.

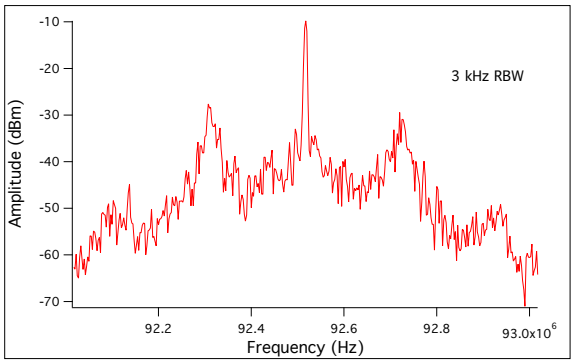

Figure 6.10: Reference servo proportional gain increased to bandwidth limit, showing bandwith of 200 kHz in the closed-loop system.

With a linewidth of 525 Hz at 1062 nm ($\sim$ 2kHz in the UV), the probe linewidth is narrow enough for Doppler spectroscopy and resolution of the recoil peaks [31]. If the system is eventually upgraded to a full lattice-based system, further reduction of the linewidth will be necessary. This can be achieved by finding the zero-expansion temperature of the UHF cavity, implementing an active temperature control system, and replacing the avalanche photodiode monitoring the UHF cavity signal with a resonant biased photodiode.

6.10 Alignment of the probe beam to the MOT

In addition to frequency considerations, we must ensure excellent spatial overlap between the probe laser beam and the MOT cloud. The spatial mode of the 265.6 nm probe light is very elliptical owing to the severe walk-off angle of the BBO crystal. We chose not to implement any complex spatial filtering, since the UV beam is not coupled into another cavity. We do use one cylindrical lens along with a telescope to collimate and focus the probe beam. Since the AR-coating on the MOT optics extends to the clock wavelength, we can easily co-propagate the probe beam with the vertical MOT beam, using a beamsplitter to combine the beams. Seeking an eventual doppler-free measurement of the recoil shift, we setup the alignment such that the incident and retro-reflected beam both overlap the MOT, with equivalent beam size at the MOT. In practice, the latter requirement of equivalent size is difficult to implement because of the highly distorted spatial mode. Regardless, the alignment works ideally with the beam focus placed at the top MOT retro-reflecting mirror. To measure the probe beam size at the approximate location of the MOT location, we use a flipper mirror to direct the beam into a free space location where we can place a a beam profiler, using path lengths equivalent to those along the actual probe-MOT interaction path. The probe beam was changed slightly between the spectroscopy measurements made with the first generation OPSL cooling laser and those made with the second generation fiber-amplified ECLD. The beam profile used during the second generation measurements seems to have impacted the level of MOT depletion observed. In Fig. 6.11, we present data for probe beam profiles

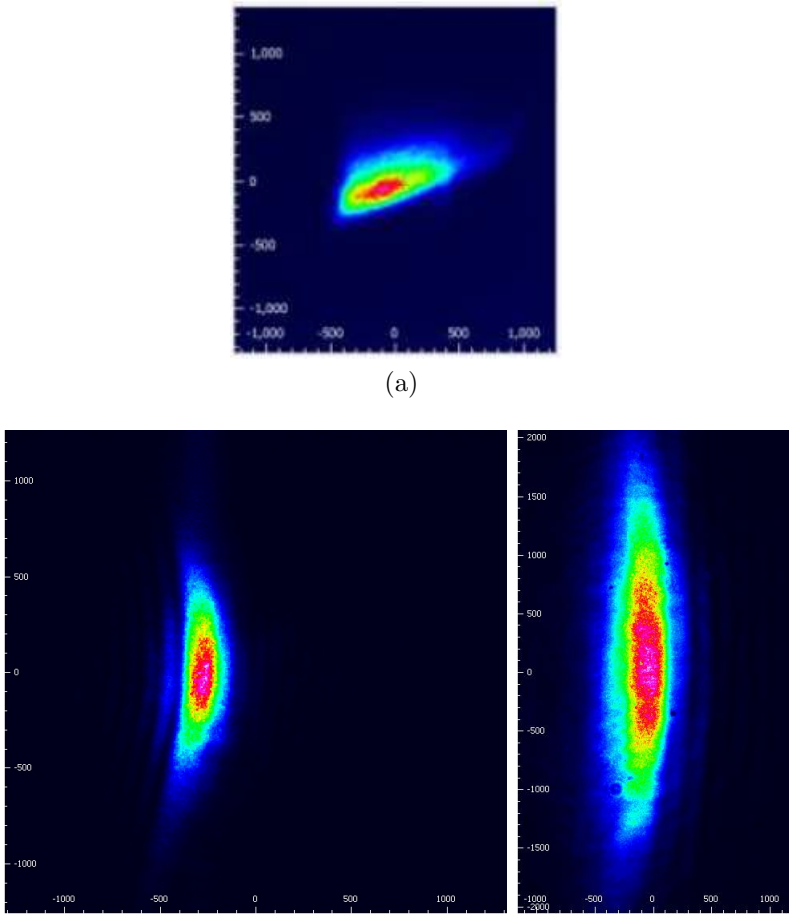

(a)

(b) (c)

Figure 6.11: (a) Incident probe beam spatial profile under the first generation measurements (TOPTICA reference laser). MOT depletion was approximately 90% at 3 mW. (b) Second generation measurements (fiber reference laser), incident beam profile; MOT depletion is 90% at 500 µW, suggesting improved overlap with the MOT cloud. (c) Second generation, return beam profile.

from both generations.

Intersecting the 200 µm diameter MOT inside "prohibited airspace" is not a trivial matter. Without access to the inside of the chamber, we devised a novel method to verify overlap of the probe beam and MOT cloud. First, the beam is

approximately aligned to the center of both vertical MOT chamber access windows. Then, while observing the MOT in real time, we place in iris in the vertical MOT beam path and adjust the aperture size and position until we only observe very weak MOT fluorescence. We then align the incident and retroreflected probe beam through this iris. This method has proved reliable and consisted for achieving spatial overlap.

6.11 Spectroscopy of the 6^1S_0 - 6^3P_0 clock transition

To scan the Hg clock transition, we apply the following method to tune the 1.1335 GHz distance from the iodine reference to the Hg transition:

(i) Find the I_2 reference transition with the probe laser. The I_2 frequency is 564285.378337 GHz.

(ii) While observing the beatnote, tune the reference laser $\pm\Delta$ MHz away from the probe laser (Δ is the distance from the I_2 frequency to ^{199}Hg frequency).

(iii) Shift the reference laser an offset $\pm$ δ MHz until we are able to lock to a TEM_{00} mode of the UHF cavity.

(iv) Tune the probe laser towards the ^{199}Hg frequency, stopping when the beat note reads frequency δ.

(v) Activate the PLL at the offset frequency δ.

(vi) Apply a slow, low amplitude FM modulation to the PLL *reference* frequency to search for the clock transition in the immediate frequency neighborhood of

offset δ.

Depending upon the distance between the Hg transition and the nearest UHF cavity mode, we may need to be able to set the phase lock offset at up to 750 MHz (one-half the FSR of the UHF cavity). The UHF cavity will of course drift over time, where as the Hg transition will not drift. We also note from the above prescription that the probe laser cannot lock to the Iodine reference while scanning the Hg transition.

Using the method outlined above, we successfully located and scanned the Hg clock transition. Figure 6.12 shows our initial scan of the clock transition. The ^{199}Hg transition frequency, as reported by Petersen [70], is 1128575.290808 GHz. During the measurement, we scanned the probe laser at a rate of 112 kHz/s (UV) and applied a 1 Hz digital low-pass filter to the PMT fluorescence signal. The filter eliminates large amplitude fluctuations from the PMT signal. The slow scan rate ensures that the MOT repopulates fast enough to prevent an asymmetric scan of the transition.

The initial measurements required 3 mW of probe power for the MOT fluorescence to be 90% depleted. Measurements with the MOT beams on continuously were also taken with the fiber-amplified ECLD and the updated spectroscopy laser. Under these conditions, the MOT was depleted 90% with only 500 µW of power. We attribute this to a different probe spatial profile during the second set of measurements, likely resulting in improved overlap with the MOT.

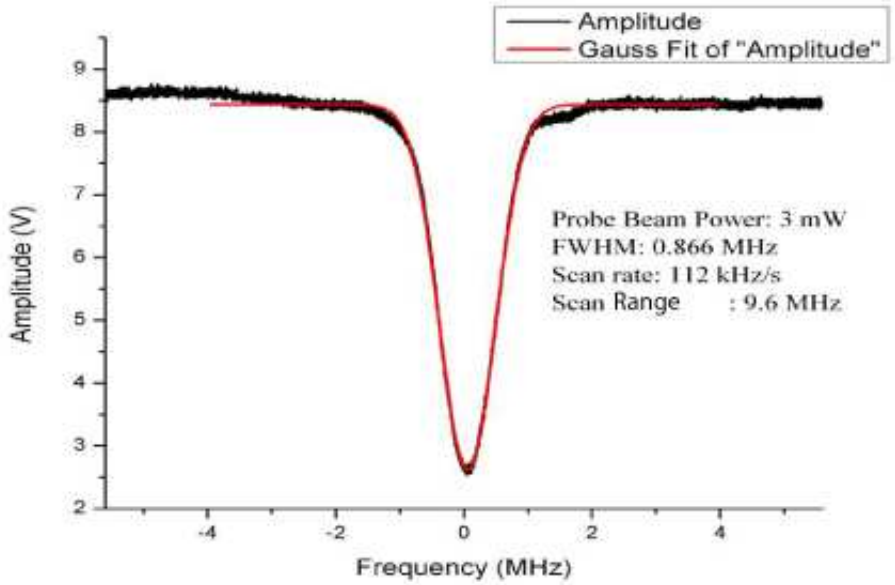

Figure 6.12: Doppler broadened clock transition spectroscopy with MOT beams running continuously.

6.12 Field-free transition spectroscopy

The spectroscopy measurement with the MOT beams on includes the significant AC stark shift induced by the MOT cooling beams. To get a more precise value for the clock transition, we want to extract the value of the stark shift. There are many other sources of clock frequency shift, including the stark shift from the probe beam, but most of these are not resolvable at the doppler level. We focus on the cooling light as it is likely to contribute a large magnitude shift that is resolvable with our spectroscopy apparatus.

To measure the Hg line free from the influence of the cooling beams, we implement a scheme to alternately cycle the cooling light and the probe laser. We

accomplish this using a chopper wheel. The chopper is inserted in the cooling beam path near the focus of the expansion telescope, before being split in front of the MOT chamber. This allows us to simultaneously shut off all arms of the cooling beams in 10 µs. The beams are chopped at a frequency of 890 Hz with a duty cycle of 50%, creating windows of time where the MOT beams were on/off for 560 µs. When the cooling beams shut off, an Arduino micro-controller board triggers an AOM which switches the probe beam onto the MOT cloud. The probe beam stays active for 500 µs. We found that 500 µs yields maximum depletion of the MOT fluorescence (30%, specifically), although this does not correspond to a π-pulse.

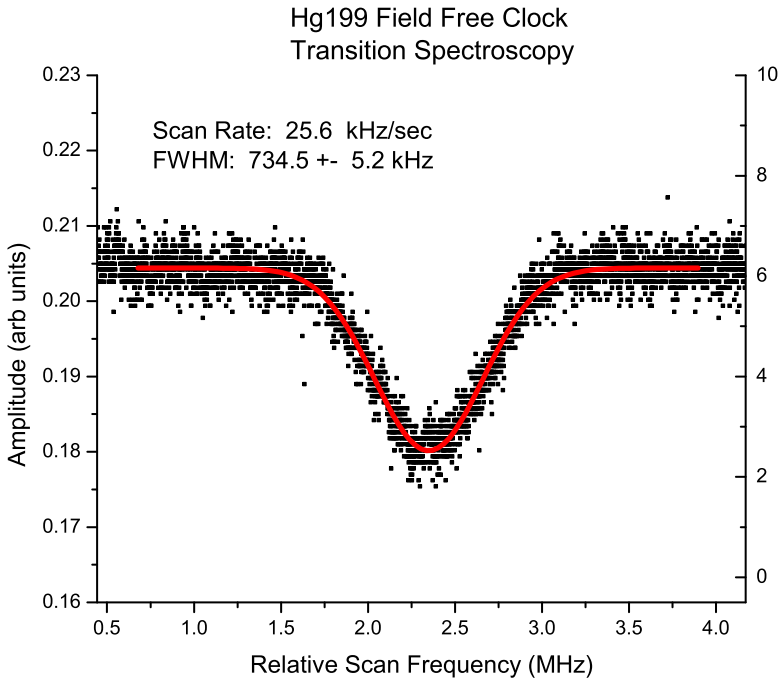

Figure 6.13: Field-free clock transition spectroscopy scan. There was no detectable difference in the doppler linewidth between the field on and the field-free measurements.

Figure 6.13 shows the results of this field-free scan of the clock transition. The frequency of the clock laser advances continuously as it periodically probes the MOT cloud according to the above prescription. The fluorescence signal is monitored with a PMT and sent through a digital low-pass filter.

Despite using a pump-probe configuration, we did not observe a Doppler recoil doublet in the transition scans. This may be due to a poor spatial profile, inadequate overlap of the pump and probe, or the linewidth of the probe laser. During these initial measurements, the linewidth of our probe laser was on the order of the free-running linewidth (7 kHz), due to the low bandwidth PZT used for correction.

6.13 Determination of the UHF cavity drift rate

Previously, we described our characterization of the UHF cavity (Sec. 6.7). Initially, we estimated the cavity drift by locking the probe laser to to the iodine reference and measuring the beatnote with the reference laser stabilized to the UHF cavity. Amplitude fluctuations in the iodine lock resulted in ± 1 MHz accuracy. A linear fit to the beatnote drift resulted in a 1.5 kHz/min drift rate in the UV. This was sufficient to pursue initial spectroscopy of the clock transition.

Following detection of the clock transition, we pursued a more accurate characterization of the cavity drift. By slowly scanning the probe frequency across the Hg transition using the phase lock local oscillator, we can observe the transition relative to the oscillator trigger. The trigger rise will drift relative to the center of the doppler profile. We measure the offset between the trigger and a guassian fit to the doppler profile, with an error of ± 5 kHz. Recording many scans over minutes

to hours allows us to characterize the frequency drift of the UHF cavity relative to the transition.

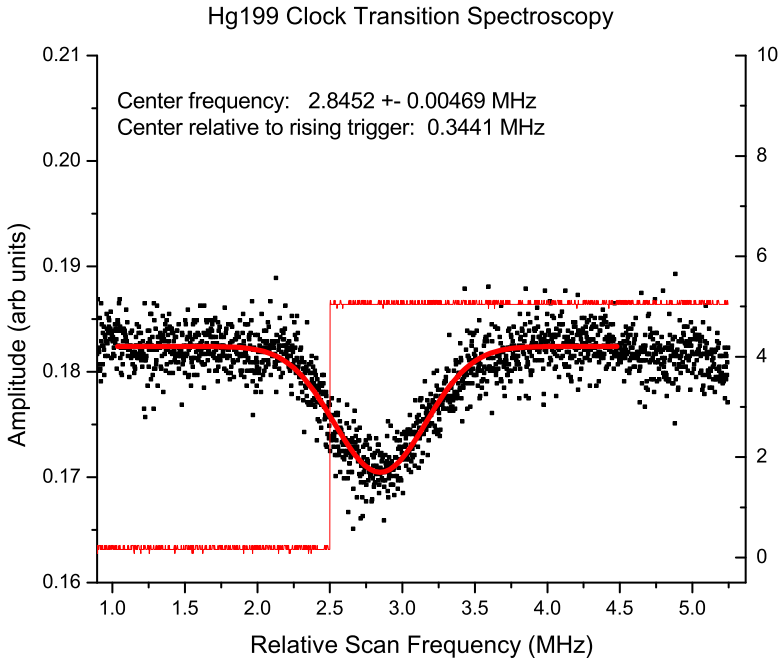

Figure 6.14: Linear drift of UHF cavity, measured relative to the Hg clock transition.

Figure 6.14 shows the data from one set of drift measurements, where we measured a linear drift of -557.7 Hz/s. Measurements at different days and times yielded a variety of different drift rates, some as low as 50 Hz/s. However, many of these sets were nonlinear over many minutes of measurement time. We attribute the inconsistent drift rates to a lack of active thermal stabilization for the UHF cavity. Ideally, the zero-expansion point of the cavity will be measured, and future iterations will incorporate thermal feedback to maintain the zero-expansion temperature. Currently, any transition measurements sensitive to the cavity drift must be accompanied with

a unique drift characterization.

6.14 Iodine reference frequency measurement

Observation of the Hg clock transition allows us to determine a higher precision value for the Iodine reference line than the one provided by the atlas [77]. To make this measurement, we first find the center clock transition frequency relative to the beatnote between the reference laser and the probe laser. We record this beatnote, and then tune the probe laser back to the iodine reference line. We then use an FM method to lock the probe laser to the iodine line, and record the beatnote frequency.

For the iodine frequency, we find a value of 564285.3783374 GHz with an uncertainty of ±360 kHz. The relatively large uncertainty originates from difficulties in producing a clean error signal from the iodine saturated absorption setup. The amount of power required to produce an acceptable SNR resulted in large amplitude fluctuations of the error signal baseline, as well as an asymmetric error signal. Figure 6.15a shows how we estimated the uncertainty. The uncertainty resulting from the asymmetry was larger than the RMS noise of the locked error signal, as well as the uncertainty in our knowledge of the frequency separation between the Hg transition and the iodine. We did not make further attempts to improve the iodine error signal, as a 360 kHz uncertainty was sufficient to reliably and consistently find the Doppler-broadened Hg transition.

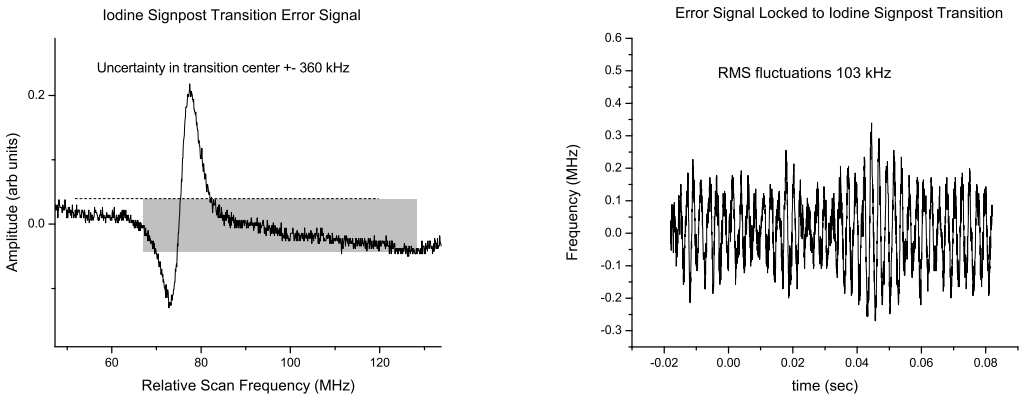

(a) (b)

Figure 6.15: (a) Estimation of the uncertainty in the I_2 error signal. (b) RMS frequency noise of the locked I_2 error signal.

6.15 MOT temperature derived from clock transition spectroscopy

As a check for our time-of-flight temperature measurements, we derived the temperature from the Doppler-broadened linewidth of the clock transition. Assuming that the Doppler-broadening is dominant, we can express the temperature of the MOT cloud as

$$T = \frac{\delta\nu_{FWHM}^2}{\nu_0^2}\frac{mc^2}{8k_B ln(2)}. \tag{6.3}$$

Another effect we must consider is the power broadening due to the probe power:

$$\Gamma(1 + \frac{I}{I_{sat}})^{1/2}. \tag{6.4}$$

At non-zero probe intensities, the spectral profile of the Hg will be a convolution of the power-broadened linewidth, the doppler linewidth, and the natural linewidth. The natural linewidth, at less than 1 Hz, can be safely disregarded. Therefore, we expect a curve that increases with the probe intensity in accordance with Eq. 6.4.

We performed several experimental runs in order to evaluate the clock linewidth at several different probe powers. These experiments were performed under two sets of conditions: (A) First-generation system (OPSL cooling laser, Toptica reference laser), field-free measurement; (B) Second generation system (fiber ECLD cooling laser, fiber reference laser), field-on measurement. Figure 6.16a shows the condition A measurements and Fig. 6.16b shows the measurements under condition B, as well as a comparison with A. The strong increase in temperature relative to power indicates a significant amount of power broadening from the probe laser. The significant error in the A measurements is a result of low SNR in the MOT fluorescence signal at these lower powers. Due to the power broadening, an accurate temperature measurement must be taken in the limit as the probe power goes to zero.

From the data, we conclude that the MOT has a temperature of 120-140 μK. This agrees well with the temperatures obtained from the time-of-flight experiments, and we are confident in the accuracy of this temperature. We conclude that our MOT is several times hotter than the Doppler limit temperature, and suspect that future improvements will be required to bring the temperature down further for the purposes of implementing a lattice clock.

6.16 AC stark shifts of the clock transition

Despite our limited resolution at the Doppler level, we decided to search for the AC stark shifts resulting from the cooling beams and the probe beam. The field-free method described earlier provides an excellent tool for measuring the cooling beam stark shift.

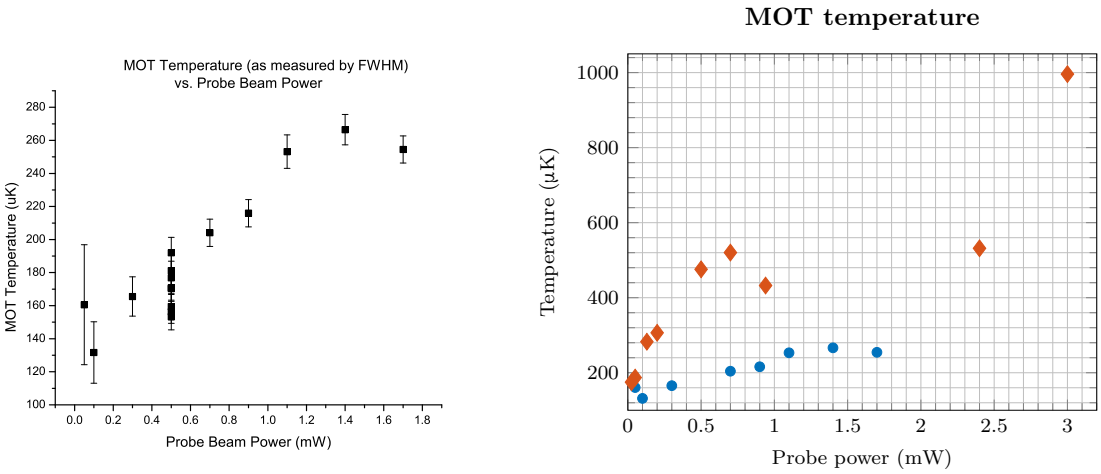

(a) (b)

Figure 6.16: MOT temperatures derived by taking the limit as the probe power goes to zero. (a)) MOT temperatures derived using the original OPSL cooling laser. (b)) MOT temperature comparison between OPSL and fiber-amplified ECLD. Blue dots represent data from the first generation OPSL-based system. Orange dots represent data from the second generation fiber ECLD system. The different probe spatial profile during the second generation results in greater power broadening at higher probe powers.

The method we used to characterize the stark shift involves making a field-on measurement of the stark shift, followed by a field-free measurement. Due to the long transition scan times required for both measurements, the cavity drift rate could easily drown out any detectable stark shifts. While switching between field-on and field-free measurements, we ensured to keep account of the cavity drift rate. The cooling beam power used during these measurements was 4.5 mW. The results of this measurement, shown in Fig. 6.17, reveal a distinct frequency shift of the clock state under the influence of the cooling beams. We also observe the expected linear drift of the cavity. The average stark shift, after subtracting the cavity drift,

is 99±8 kHz. Figure 6.17b shows an individual scan measurement, with the field-on and field-free scans juxtaposed. The blue stark-shift of the clock transition is shown.

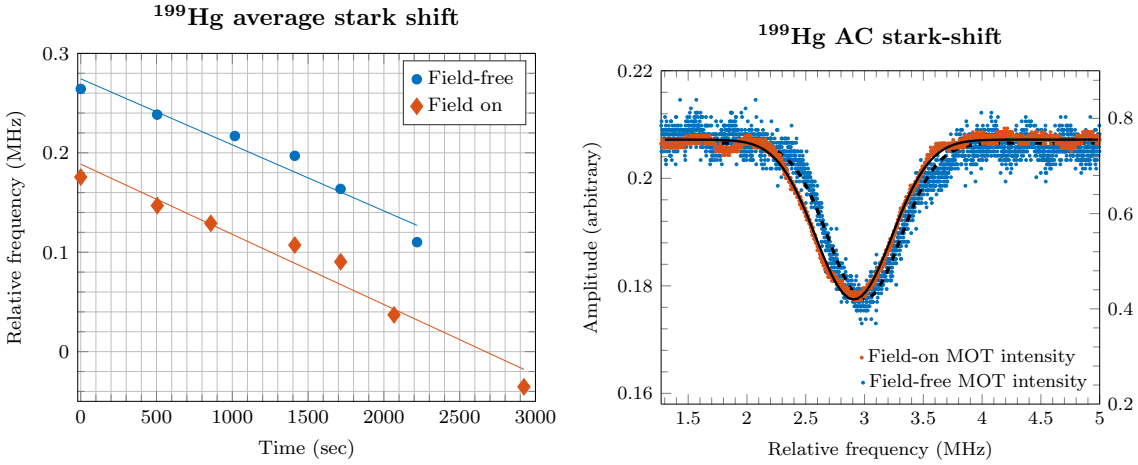

(a) (b)

Figure 6.17: AC stark shift of the clock transition. Average stark shift of 100 kHz is measured.

We attempted to measure the stark shift from the probe laser (266 nm), but were unable to detect a shift. This is not unexpected, since the literature [33] indicates the magnitude of the probe shift is well below the ∼10 kHz linewidth of our probe laser. More details of this measurement can be found in the thesis of Justin Paul [71].

6.17 Additional measurements: Photon recoil and two-photon spectroscopy

After upgrading the cooling laser to the fiber-amplified ECLD system and verifying we could perform basic spectroscopy of the clock line, we set about to perform two measurements: search for the photon recoil and the two-photon transition in

mercury. The photon recoil has been observed previously by Petersen et. al. [31]. They found the recoil peaks were separated by about 35 kHz in the UV. With our upgraded spectroscopy system, we are confident the probe laser linewidth is around 2 kHz in the UV, which is more than sufficient to resolve the recoil peaks. However, after setting up the spectroscopy system for very slow scans of the transition, we were unable to resolve the recoil peaks. We suspect this may be due to either the poor probe beam spatial profile or the lack of active temperature stabilization for the UHF cavity. The poor probe profile may result in a sub-optimal overlap between the incident and retro-reflected probe beams inside the MOT chamber, causing low SNR for a doppler-free measurement. Lack of active temperature stabilization results in an uncontrolled drift rate of the probe laser, making it very difficult to implement the slow scans necessary to resolve kilohertz-level features.

Despite our inability to resolve the photon recoil peaks, we decided to implement several upgrades to our experiment that would allow us to attempt a measurement of the two-photon transition in neutral mercury. A published analysis by Alden et. al. [79] highlights the potential for a room-temperature mercury vapor clock, exploiting the two-photon E1-M1 clock transition. However, an experimental attempt to detect the transition at room temperature failed, likely due to technical difficulties in directly interrogating the clock transition. A cold atom mercury system gives us the ability to probe the two-photon transition using the indirect MOT depletion spectroscopy we used for the clock transition. This is a much more sensitive detection method than attempting to directly read out the clock level using one of the upper-lying Hg states. Although we failed to detect the two photon transition, in

this section we describe the modifications made to our setup to help facilitate the measurement attempt.

Prior to performing the experiment, we estimated the signal magnitude (i.e. percentage of dip in fluorescence of the steady-state MOT) we would expect from scanning the two-photon transition with 500 mW of power at 531 nm. To determine this, we need to know the probability of two-photon excitation to the $^3\mathrm{P}_0$ level. From Alden [80], this probability is given by:

$$P_{^3P_0} = \frac{\dot{N}_{^3P_0}(T, \omega_0)}{\dot{N}_{tot}(T, \omega_0)} \tag{6.5}$$

where $\dot{N}_{^3P_0}$ is the rate of atoms excited to the $^3P_0$ level and $\dot{N}_{tot}$ is the rate of atoms flowing through the interrogation region.

This probability is related to the two-photon Rabi frequency, but first we must determine whether our experiment will be time-limited or velocity-limited. In the time-limited regime, the transit-time broadening dominates the residual first-order Doppler broadening ($\Delta\nu_{TT} > \Delta\nu_D$); in the velocity-limited regime, the opposite is true ($\Delta\nu_D > \Delta\nu_{TT}$). Transit time is given by:

$$\bar{t} = 2\omega_0 \times \sqrt{\frac{\pi M}{8k_B T}}. \tag{6.6}$$

In a Doppler-free two-photon experiment, residual Doppler broadening results from angular misalignment between the counterpropogating beams. Alden [80] reports the residual broadening for mercury (valid for small misalignment angles):

$$\Delta\nu_D = 1.9 \times 10^7 \sqrt{T} \times \theta. \tag{6.7}$$

Assuming a MOT temperature, T, of 120 µK, and a beam waist, ω_0, of 100 µm (approximately equivalent to the MOT diameter of 200 µm), we estimate, using

Eq. 6.6 ($\Delta\nu_{TT} = 1/\bar{t}$), a transit time of 545 Hz. An angular misalignment of 10 milliradians results in a residual doppler broadening of 2 kHz. Since we did not measure the angles between the counterpropogating beams, we assume the doppler broadening is dominant. In a room-temperature system, the transit time would dominate the broadening by a wide margin, assuming reasonable minimization of the alignment angle.

For the Doppler regime, Alden [80] gives the probabillity of excitation to the clock state:

$$P_{^3P_0}(T, \omega_0) \approx \frac{\Omega_{R2\gamma}^2}{\Delta\nu_D^2}, \tag{6.8}$$

where $\Omega_{R2\gamma} = 9.3 \times 10^{-6} \times I$. Assuming an incident power of 500 mW and corresponding intensity at the MOT of approximately 30 MW/m^2, we calculate a 2% probability of two-photon excitation to the clock state. This assumes a residual Doppler broadening of 2 kHz, which matches well with our probe laser linewidth of 2 kHz (in the UV). With adequate filtering and averaging of the signal, a 2% dip in MOT fluroescence should be detectable with our current setup.

Under the original experimental setup, we only generate 150 mW at the 531 nm two-photon wavelength. To boost this power, we built a 1062 nm ytterbium amplifier to insert after the commercial Nufern amplifier and the fiber-coupled AOM (see Fig. 6.1). For this system we use 2 m of Yb-doped PM gain fiber. The 1062 nm light from the AOM is coupled out into free-space, passes through an EOT isolator, and is then coupled into the gain fiber using an 11.2 mm aspheric lens. At the output of the gain fiber, we insert a dichroic to separate out the excess pump light. We are able to generate 4.3 W at 1062 nm, beyond which the amplifier output saturates.

We then send the light through an OFR isolator and use a 12.5 cm lens to focus into the PPLN. With 4.3 W of incident power, we generate 640 mW at 531 nm. We then insert a high-power $\lambda/2$ waveplate and a polarizing beam splitter as a switch, so we can easily divert 531 nm light to the chamber after finding the transition with the UV light. Since the MOT optics are not AR-coated at green wavelengths, we must align the green beam such that it overlaps with the MOT without being required to pass through any UV optics. To accomplish this, we split off a small amount of UV probe power, then create a path for that beam into the MOT which avoids the MOT optics. This alignment is most easily performed with the probe light on resonance while observing the MOT depletion in real-time.

Despite careful alignment of the system, we were unable to observe the two-photon transition. This may be due to lack of sufficient intensity, uncontrolled drift of the UHF cavity, or poor SNR. We recommend implementing active thermal control of the UHF cavity before making future attempts at the two-photon measurement.

CHAPTER 7

Summary and conclusion

In this dissertation I have described in detail our efforts to develop the components of an optical atomic clock based on neutral mercury. While we do not have a fully implemented lattice clock, we have built several of the primary systems typically used in a clock. These systems include the cooling laser, the spectroscopy laser, the ultra-stable cavity, and the MOT chamber.

We first demonstrated a laser based on optically-pumped semiconductors (OPSL) that can generate over 1.5 W at 1014.9 nm. Using an intra-cavity etalon and birefringient filter, we can tune the OPSL wavelength over several nanometers and force lasing on a single mode. With two intracavity doubling stages placed downstream from the cavity, we can generate over 100 mW at the 254 nm wavelength of the intercombination cooling line in mercury.

Seeking a replacement for the OPSL laser system, we have constructed a fiber-amplified ECLD system that generates up to 6 W of power at 1014.9 nm. The amplifier consists of two stages and uses short sections of gain fiber in order to minimize ASE power. The first stage seeds the second stage with 500 mW of power. Any excess ASE at the output of the second stage is filtered via the downstream doubling cavities. After integrating the amplifier with the doubling cavities, we are able to generate over 100 mW at 254 nm. Both the OPSL and the fiber amplifier

source have been used to trap and cool the ^{199}Hg isotope.

To perform spectroscopy on the clock transition, we have constructed a stabilized spectroscopy laser. The laser is locked to an ultra-high finesse optical cavity with a finesse of 600,000, and can reach a linewidth as low as 525 Hz in the IR. This is insufficient for sub-doppler spectroscopy, but allowed us to scan and measure the doppler broadened clock line. To find the clock transition in frequency space, we used an iodine reference transition approximately 1.1 GHz away from the clock transition.

In addition to measuring the Doppler-broadened clock transition, we performed measurements to characterize the stark shifts resulting from the cooling laser and the probe (spectroscopy) laser. We detected a stark shift of 100 kHz due to the cooling laser, but were unable to resolve any shift from the probe laser. We characterized the drift rate of the ultra-high finesse cavity, and discovered that the rate was highly variable. We expect improvements to the temperature control system of the cavity will eliminate this variability.

Finally, we have attempted two measurements that seek to resolve sub-doppler features. The first measurement sought to detect the photon recoil peaks. While our laser linewidth should be sufficiently small to resolve the recoil features, we were unable to detect these peaks. The second measurement was an attempt to detect the two-photon transition in mercury. We increased the power of the intermediate 531 nm light in our spectroscopy system, diverted it towards the MOT chamber, and attempted to scan the two-photon transition. Unfortunately, we did not detect a signal.

REFERENCES

[1] M. Grewal, A. Andrews, and C. Bartone, *Global Navigation Satellite Systems, Inertial Navigation, and Integration*. John Wiley & Sons, New York, 2013.

[2] E. Kaplan and C. Hegarty, *Understanding GPS: Principles and Applications*. Artech House Publishers, Norwood, MA, 2006.

[3] F. Walls and J. Vig *IEEE Trans. Ultrason. Ferroelectr. Frq. Control*, vol. 42, p. 576, 1995.

[4] L. Judah, "A review of time and frequency transfer methods," *Metrologia*, vol. 45, no. 6, p. S162, 2008.

[5] W. Markowitz, R. G. Hall, L. Essen, and J. V. L. Parry, "Frequency of cesium in terms of ephemeris time," *Phys. Rev. Lett.*, vol. 1, pp. 105–107, Aug 1958.

[6] B. N. Taylor and A. Thompson, "The International System of Units (SI)." Online, 2008.

[7] N. Hinkley, J. A. Sherman, N. B. Phillips, M. Schioppo, N. D. Lemke, K. Beloy, M. Pizzocaro, C. W. Oates, and A. D. Ludlow, "An Atomic Clock with 10^{-18} Instability," *Science*, vol. 341, pp. 1215–1218, 2013.

[8] J. A. Barnes, A. R. Chi, L. S. Cutler, D. J. Healey, D. B. Leeson, T. E. McGunigal, J. A. Mullen, W. L. Smith, R. L. Sydnor, R. F. C. Vessot, and

G. M. R. Winkler, "Characterization of Frequency Stability," *IEEE Trans. Instrum. Meas.*, vol. IM-20, pp. 105–120, 1971.

[9] W. J. Riley, *Handbook of Frequency Stability Analysis*, vol. 31. 1994.

[10] D. W. Allan, "Statistics of Atomic Frequency Standards," *Proceedings of the IEEE*, vol. 54, no. 2, pp. 221–230, 1966.

[11] A. D. Ludlow, M. M. Boyd, J. Ye, E. Peik, and P. O. Schmidt, "Optical Atomic Clocks," *Preprint at arxiv.org/abs/1407.3493 (to appear on Rev. Mod. Phys.)*, pp. 1–86, 2015.

[12] W. M. Itano, J. C. Bergquist, J. J. Bollinger, J. M. Gilligan, D. J. Heinzen, F. L. Moore, M. G. Raizen, and D. J. Wineland, "Quantum projection noise: Population fluctuations in two-level systems," *Physical Review A*, vol. 47, no. 5, pp. 3554–3570, 1993.

[13] S. A. Diddams, T. Udem, J. C. Bergquist, E. A. Curtis, R. E. Drullinger, L. Hollberg, W. M. Itano, W. D. Lee, C. W. Oates, K. R. Vogel, and D. J. Wineland1, "An Optical Clock Based on a Single Trapped $^{199}Hg^{+}$ Ion," *Science*, vol. 293, pp. 825–828, 2001.

[14] D. A. Jennings, K. M. Evenson, and D. J. E. Knight, "Optical frequency measurements," *Proceedings of the IEEE*, vol. 74, pp. 168–179, Jan 1986.

[15] H. Schnatz, B. Lipphardt, J. Helmcke, F. Riehle, and G. Zinner, "First phase-coherent frequency measurement of visible radiation," *Phys. Rev. Lett.*, vol. 76, pp. 18–21, Jan 1996.

[16] J. L. Hall, "Nobel lecture: Defining and measuring optical frequencies*," *Rev. Mod. Phys.*, vol. 78, pp. 1279–1295, Nov 2006.

[17] T. W. Hänsch, "Nobel lecture: Passion for precision*," *Rev. Mod. Phys.*, vol. 78, pp. 1297–1309, Nov 2006.

[18] S. A. Diddams, D. J. Jones, J. Ye, S. T. Cundiff, J. L. Hall, J. K. Ranka, R. S. Windeler, R. Holzwarth, T. Udem, and T. W. Hänsch, "Direct link between microwave and optical frequencies with a 300 thz femtosecond laser comb," *Phys. Rev. Lett.*, vol. 84, pp. 5102–5105, May 2000.

[19] D. J. Jones, S. A. Diddams, J. K. Ranka, A. Stentz, R. S. Windeler, J. L. Hall, and S. T. Cundiff, "Carrier-envelope phase control of femtosecond mode-locked lasers and direct optical frequency synthesis," *Science*, vol. 288, no. 5466, pp. 635–639, 2000.

[20] S. T. Cundiff and J. Ye, "*Colloquium* : Femtosecond optical frequency combs," *Rev. Mod. Phys.*, vol. 75, pp. 325–342, Mar 2003.

[21] L.-S. Ma, Z. Bi, A. Bartels, L. Robertsson, M. Zucco, R. S. Windeler, G. Wilpers, C. Oates, L. Hollberg, and S. A. Diddams, "Optical frequency synthesis and comparison with uncertainty at the 10-19 level," *Science*, vol. 303, no. 5665, pp. 1843–1845, 2004.

[22] H. Inaba, K. Hosaka, M. Yasuda, Y. Nakajima, K. Iwakuni, D. Akamatsu, S. Okubo, T. Kohno, A. Onae, and F.-L. Hong, "Spectroscopy of 171yb in

an optical lattice based on laser linewidth transfer using a narrow linewidth frequency comb," *Opt. Express*, vol. 21, pp. 7891–7896, Apr 2013.

[23] T. Rosenband, D. B. Hume, P. O. Schmidt, C. W. Chou, a. Brusch, L. Lorini, W. H. Oskay, R. E. Drullinger, T. M. Fortier, J. E. Stalnaker, S. a. Diddams, W. C. Swann, N. R. Newbury, W. M. Itano, D. J. Wineland, and J. C. Bergquist, "Frequency Ratio of Al+ and Hg+ Single-Ion Optical Clocks; Metrology at the 17th Decimal Place," *Science*, vol. 319, no. 5871, pp. 1808–1812, 2008.

[24] C. W. Chou, D. B. Hume, J. C. J. Koelemeij, D. J. Wineland, and T. Rosenband, "Frequency Comparison of Two High-Accuracy Al^+ Optical Clocks," *Phys. Rev. Lett.*, vol. 104, p. 070802, Feb 2010.

[25] K. Matsubara, H. Hachisu, Y. Li, S. Nagano, C. Locke, A. Nogami, M. Kajita, K. Hayasaka, T. Ido, and M. Hosokawa, "Direct comparison of a ca+ single-ion clock against a sr lattice clock to verify the absolute frequency measurement," *Opt. Express*, vol. 20, pp. 22034–22041, Sep 2012.

[26] P. Dubé, A. A. Madej, M. Tibbo, and J. E. Bernard, "High-Accuracy Measurement of the Differential Scalar Polarizability of a $^{88}Sr^+$ Clock Using the Time-Dilation Effect," *Phys. Rev. Lett.*, vol. 112, p. 173002, Apr 2014.

[27] N. Huntemann, B. Lipphardt, C. Tamm, V. Gerginov, S. Weyers, and E. Peik, "Improved Limit on a Temporal Variation of m_p/m_e from Comparisons of Yb^+ and Cs Atomic Clocks," *Phys. Rev. Lett.*, vol. 113, p. 210802, Nov 2014.

[28] J. C. Bergquist, W. M. Itano, and D. J. Wineland, "Recoilless optical absorption and doppler sidebands of a single trapped ion," *Phys. Rev. A*, vol. 36, pp. 428–430, Jul 1987.

[29] H. Hachisu, K. Miyagishi, S. G. Porsev, A. Derevianko, V. D. Ovsiannikov, V. G. Pal'chikov, M. Takamoto, and H. Katori, "Trapping of neutral mercury atoms and prospects for optical lattice clocks," *Physical Review Letters*, vol. 100, no. 5, 2008.

[30] K. Yamanaka, N. Ohmae, I. Ushijima, M. Takamoto, and H. Katori, "Frequency Ratio of ^{199}Hg and ^{87}Sr Optical Lattice Clocks beyond the SI Limit," *Phys. Rev. Lett.*, vol. 114, no. 23, p. 230801, 2015.

[31] M. Petersen, R. Chicireanu, S. T. Dawkins, D. V. Magalhães, C. Mandache, Y. Le Coq, A. Clairon, and S. Bize, "Doppler-free spectroscopy of the S01-P03 optical clock transition in laser-cooled fermionic isotopes of neutral mercury," *Physical Review Letters*, vol. 101, no. 18, 2008.

[32] *Magneto-Optical Trap of Neutral Mercury for an Optical Lattice Clock*, IEEE International Frequency Control Symposium, 2008.

[33] J. J. McFerran, L. Yi, S. Mejri, S. Di Manno, W. Zhang, J. Guéna, Y. Le Coq, and S. Bize, "Neutral atom frequency reference in the deep ultraviolet with fractional uncertainty=5.7×10^{-15}," *Physical Review Letters*, vol. 108, no. 18, 2012.

[34] J. J. McFerran, L. Yi, S. Mejri, W. Zhang, S. Di Manno, M. Abgrall, J. Guena,

Y. Le Coq, and S. Bize, "Statistical uncertainty of 2.5 x 10(-16) for the Hg-199 S-1(0)-P-3(0) clock transition against a primary frequency standard," *PHYSICAL REVIEW A*, vol. 89, APR 30 2014.

[35] M. Scheid, F. Markert, J. Walz, J. Wang, M. Kirchner, and T. W. Hänsch, "750 mW continuous-wave solid-state deep ultraviolet laser source at the 253.7 nm transition in mercury.," *Optics letters*, vol. 32, no. 8, pp. 955–957, 2007.

[36] B. Cocqquelin, G. Lucas-Leclin, P. George, I. Sagnes, and A. Garanche, "Single-frequency tunable VECSEL around the Cesium D_2 line," *Solid State Lasers XVII:Technology and Devices, Proc. SPIE*, vol. 6871, 2008.

[37] J. Paul, Y. Kaneda, T.-L. Wang, C. Lytle, J. V. Moloney, and R. J. Jones, "Doppler-free spectroscopy of mercury at 253.7 nm using a high-power, frequency-quadrupled, optically pumped external-cavity semiconductor laser.," *Optics letters*, vol. 36, no. 1, pp. 61–63, 2011.

[38] S. Ranta, M. Tavast, T. Leinonen, R. Epstein, and and M. Guina, "Narrow linewidth 1118/559 nm VECSEL based on strain compensated GaInAs/GaAs quantum-wells for laser cooling of Mg-ions," *Optical Materials Express*, vol. 2, pp. 1011–1019, 2012.

[39] A. Laurain, C. Mart, J. Hader, J. V. Moloney, B. Kunert, and W. Stolz, "Optical noise of stabilized high-power single frequency optically pumped semiconductor laser," *Optics Letters*, vol. 39, pp. 1573–1576, 2014.

[40] M. Kuznetsov, F. Hakimi, R. Sprague, and A. Mooradian, "Design and characteristics of high-power (0.5-W CW) diode-pumped vertical-external-cavity surface-emitting semiconductor lasers with circular TEM-00 beams," *IEEE Journal of Selected Topics in Quantum Electronics*, vol. 5, pp. 561–573, 1999.

[41] S. Lutgen, T. Albrecht, P. Brick, W. Reill, J. Luft, and W. Späth, "8-W high-efficiency continuous-wave semiconductor disk laser at 1000 nm," *Applied Physics Letters*, vol. 82, 2003.

[42] M. Jacquemet, M. Domenech, G. Lucas-Leclin, P. Georges, J. Dion, M. Strassner, I. Sagnes, and A. Garnache, "Single-Frequency cw vertical external cavity surface emitting semiconductor laser at 1003 nm and 501 nm by intracavity frequency doubling," *Applied Physics B*, vol. 86, pp. 503–510, 2007.

[43] D. Paboeuf, P. J. Schlosser, and J. E. Hastie, "Frequency stabilization of an ultraviolet semiconductor disk laser," *Optics Letters*, vol. 38, pp. 1736–1738, 2013.

[44] A. Laurain, M. Myara, G. Beaudoin, I. Sagnes, and A. Garnache, "High power single-frequency continuously-tunable compact extended cavity semiconductor laser," *Optics Express*, vol. 17, pp. 9503–9508, 2009.

[45] M. Holm, D. Burns, and A. Ferguson, "Actively Stabilized Single-Frequency Vertical-External-Cavity AlGaAs Laser," *IEEE Photon. Technol. Lett.*, vol. 11, pp. 1551–1553, 2004.

[46] R. Abram, K. Gardner, E. Riis, and A. Ferguson, "Narrow linewidth operation

of a tunable optically pumped semiconductor laser," *Optics Express*, vol. 12, pp. 5434–5439, 2004.

[47] Y. Kaneda, J. M. Yarborough, L. Li, N. Peyghambarian, L. Fan, C. Hessenius, M. Fallahi, J. Hader, J. V. Moloney, Y. Honda, M. Nishioka, Y. Shimizu, K. Miyazono, H. Shimatani, M. Yoshimura, Y. Mori, Y. Kitaoka, and T. Sasaki, "Continuous-wave all-solid-state 244 nm deep-ultraviolet laser source by fourth-harmonic generation of an optically pumped semiconductor laser using CsLiB-6O-10 in an external resonator," *Optics Letters*, vol. 33, pp. 1705–1707, 2008.

[48] T.-L. Wang, "High-Power Optically Pumped Semiconductor Lasers For Near Infrared Wavelengths." Dissertation (Ph.D.), 2012.

[49] J. V. Moloney, J. Hader, and S. W. Koch, "Quantum design of semiconductor active materials: laser and amplifier applications," *Laser and Photonics Review*, vol. 1, pp. 24–43, 2007.

[50] A. Chernikov, J. Herrmann, M. Koch, B. Kunert, W. Stolz, S. Chatterjee, S. W. Koch, T.-L. Wang, Y. Kaneda, J. M. Yarborough, J. Hader, and J. V. Moloney, "Heat Management in High-Power Vertical-External-Cavity Surface-Emitting Lasers," *IEEE Journal of Selected Topics in Quantum Electronics*, vol. 17, pp. 1772–1778, 2011.

[51] Z. Y. Ou, S. E. Pereira, E. S. Polzik, and H. J. Kimble, "85% Efficiency for CW Frequency Doubling from 1.08 to 0.54 μm," *Optical Letters*, vol. 17, pp. 640–642, 1992.

[52] G. A. Boyd and D. A. Kleinmann, "Parametric Interaction of Focused Gaussian Light Beams," *Journal of Applied Physics*, vol. 39, pp. 3597–3639, 1968.

[53] T. W. Hansch and B. Couillaud, "Laser Frequency Stabilization by Polarization, Spectroscopy of a Reflecting Reference Cavity," *Optics Communications*, vol. 35, pp. 441–444, 1980.

[54] K. Kondo, M. Oka, H. Wada, T. Fukui, N. Umezu, K. Tatsuki, and S. Kubota, "Demonstration of long-term reliability of a 266-nm, continuous-wave, frequency-quadrupled solid-state laser using β-BaB-2O-4," *Optics Letters*, vol. 23, pp. 195–197, 1998.

[55] F. Bitter, "Magnetic Resonance in Radiating or Absorbing Atoms," *Applied Optics*, vol. 1, pp. 1–10, 1962.

[56] C. Yang, S. Xu, Q. Yang, W. Lin, S. Mo, C. Li, Z. Feng, D. Chen, Z. Yang, and Z. Jiang, "High-efficiency watt-level 1014nm single-frequency laser based on short Yb-doped phosphate fiber amplifiers," vol. 062702, 1882.

[57] J. Hu, L. Zhang, H. Liu, K. Liu, Z. Xu, and Y. Feng, "High power room temperature 1014.8 nm Yb fiber amplifier and frequency quadrupling to 253.7 nm for laser cooling of mercury atoms," *Optics Express*, vol. 1, no. 25, pp. 355–357, 2013.

[58] J. Hu, L. Zhang, H. Liu, K. Liu, Z. Xu, and Y. Feng, "High-power single-frequency 1014.8 nm Yb-doped fiber amplifier working at room temperature," *Applied Optics*, vol. 53, p. 4972, 2014.

[59] K. S. Tsang, R. Man, H. Y. Tam, C. Lu, and P. K. A. Wai, "Optimal design of double-clad ytterbium-doped fiber amplifiers operating at 1020-1070," in *Pacific Rim Conference on Lasers and Electro-Optics, CLEO - Technical Digest*, 2009.

[60] Y. Jeong, J. Sahu, D. Payne, and J. Nilsson, "Ytterbium-doped large-core fibre laser with 1 kW of continuous-wave output power," *Electronics Letters*, vol. 40, p. 470, 2004.

[61] R. Paschotta, J. Nilsson, A. C. Tropper, and D. C. Hanna, "Ytterbium-doped fiber amplifiers," *IEEE Journal of Quantum Electronics*, vol. 33, no. 7, pp. 1049–1056, 1997.

[62] C. Giles and E. Desurvire, "Modeling erbium-doped fiber amplifiers," *Journal of Lightwave Technology*, vol. 9, no. 2, pp. 271–283, 1991.

[63] R. Oron and A. a. Hardy, "Rayleigh backscattering and amplified spontaneous emission in high-power ytterbium-doped fiber amplifiers," *Journal of the Optical Society of America B*, vol. 16, no. 5, p. 695, 1999.

[64] A. A. Hardy and R. Oron, "Amplified spontaneous emission and Rayleigh backscattering in strongly pumped fiber amplifiers," *Journal of Lightwave Technology*, vol. 16, no. 10, pp. 1865–1873, 1998.

[65] A. Hardy and R. Oron, "Signal amplification in strongly pumped fiber amplifiers," *IEEE Journal of Quantum Electronics*, vol. 33, no. 3, pp. 307–313, 1997.

[66] A. Seifert, M. Sinther, T. Walther, and E. S. Fry, "Narrow-linewidth, multi-Watt Yb-doped fiber amplifier at 1014.8 nm.," *Applied optics*, vol. 45, no. 30, pp. 7908–11, 2006.

[67] R. Steinborn, A. Koglbauer, P. Bachor, T. Diehl, D. Kolbe, M. Stappel, and J. Walz, "A continuous wave 10 W cryogenic fiber amplifier at 1015 nm and frequency quadrupling to 254 nm.," *Optics Express*, vol. 21, no. 19, pp. 22693–8, 2013.

[68] A. Noble and M. Kasevich, "UHV optical window seal to conflat knife edge," *Rev. Sci. Instrum.*, vol. 65, p. 3042, 1994.

[69] H. J. Metcalf and P. V. D. Straten, *Laser Cooling and Trapping*. Springer-Verlag New York Inc., 1999.

[70] M. Petersen, "Laser-cooling of Neutral Mercury and Laser Spectroscopy of the $^1S_0$ - $^3P_0$ Optical Clock Transition." Dissertation (Ph.D.), 2009.

[71] J. R. Paul, "Construction and Characterization of a Neutral Hg Magneto-Optical Trap and Precision Spectroscopy of the 6^1S_0 - 6^3P_0 Hg Clock Transition."

[72] P. Villwock, S. Siol, and T. Walther, "Magneto-optical trapping of neutral mercury," *European Physical Journal D*, vol. 65, no. 1-2, pp. 251–255, 2011.

[73] N. Instruments, "2-D Nonlinear Curve Fitting." Online NI Discussion Forums, 2010.

[74] K. E. Gibble, S. Kasapi, and S. Chu, "Improved magneto-optic trapping in a vapor cell," *Optics Letters*, vol. 17, pp. 526–528, 1992.

[75] I. Courtillot, A. Quessada, R. P. Kovacich, A. Brusch, D. Kolker, J.-J. Zondy, G. D. Rovera, and P. Lemonde, "Clock transition for a future optical frequency standard with trapped atoms," *Phys. Rev. A*, vol. 68, p. 030501(R), 2003.

[76] C. W. Hoyt, Z. W. Barber, C. W. Oates, T. M. Fortier, S. A. Diddams, and L. Hollberg, "Observation and Absolute Frequency Measurements of the $^1S_0$-$^3P_0$ Optical Clock Transition in Neutral Ytterbium," *Phys. Rev. Lett.*, vol. 95, p. 83003, 2005.

[77] H. Kato, M. Baba, S. Kasahara, K. Ishikawa, M. Misono, Y. Kimura, J. O'Reilly, H. Kuwano, T. Shimamoto, T. Shinano, C. Fujiwara, M. Ikeuchi, N. Fujita, M. H. Kabir, M. Ushino, R. Takahashi, and Y. Matsunobu, *Doppler-Free High Resolution Spectral Atlas of Iodine Molecule 15000-19000 cm^{-1}*. Japan Society for the Promotion of Science, 2000.

[78] J. Alnis, A. Matveev, N. Kolachevsky, T. Udem, and T. W. Hänsch, "Subhertz linewidth diode lasers by stabilization to vibrationally and thermally compensated ultralow-expansion glass Fabry-Perot cavities," *Physical Review A*, vol. 77, no. 5, 2008.

[79] E. A. Alden, K. R. Moore, and A. E. Leanhardt, "Two-photon E1-M1 optical clock," *Phys. Rev. A*, vol. 90, p. 12523, jul 2014.

[80] E. A. Alden, "A Two-Photon E1-M1 Optical Clock."